Title
Tuning the Optical Response of Graphene and Metamaterials

Author
Goldflam, Michael

Publication Date
2015

Peer reviewed|Thesis/dissertation

UNIVERSITY OF CALIFORNIA, SAN DIEGO

Tuning the Optical Response of Graphene and Metamaterials

A dissertation submitted in partial satisfaction of the
requirements for the degree
Doctor of Philosophy

in

Physics

by

Michael David Goldflam

Committee in charge:

Professor Dimitri N. Basov, Chair
Professor Michael Fogler
Professor Zhaowei Liu
Professor Oleg Shpyrko
Professor Andrea Tao

2015

The dissertation of Michael David Goldflam is approved, and it is acceptable in quality and form for publication on microfilm and electronically:

_____

_____

_____

_____

_____
Chair

University of California, San Diego

2015

EPIGRAPH

They didn't want it good,
they wanted it Wednesday.
—Robert A. Heinlein

TABLE OF CONTENTS

LIST OF FIGURES

ACKNOWLEDGEMENTS

I would like to acknowledge my family, my parents, Rudolf and Tamar Goldflam, and my sisters, Anat and Ilana. They've been there to help me throughout my life and without them, I would not have made it into, let alone through graduate school. They have supported me throughout and I owe them a great deal.

I would also like to acknowledge my advisor, Dmitri Basov, my success in graduate school is in no small part due to his continuous guidance and feedback on my work. Without his unending dedication to research and his students, I would not have had the opportunities I had in graduate school. I would also like to thank my committee members: Michael Fogler, Zhaowei Liu, Oleg Shpyrko, and Andrea Tao.

I also want to thank my group members and friends for their support in both research and in life. Kirk Post, has been my officemate for my whole time at UCSD, kept our office decorated with surf boards and was always willing to have discussions. My friends have shared countless hours of fun during my time in San Diego.

Lastly, I want to thank Leandra Boucheron for dealing with me for many years and for her never-ending support and patience.

Chapter 2, in full, is a reprint of material as it appears in M. D. Goldflam, T. Driscoll, B. Chapler, O. Khatib, N. Marie Jokerst, S. Palit, D. R. Smith, B.-J. Kim, G. Seo, H.-T. Kim, M. D. Ventra, and D. N. Basov. "Reconfigurable gradient index using VO_2 memory metamaterials," *Applied Physics Letters*, 99(4):044103, Jul. 2011. The dissertation author was the primary investigator and author of this publication.

Chapter 3, in full, is a reprint of material as it appears in M. D. Goldflam, T. Driscoll, D. Barnas, O. Khatib, M. Royal, N. M. Jokerst, D. R. Smith, B.-J. Kim, G. Seo, H.-T. Kim, and D. N. Basov. "Two-dimensional reconfigurable gradient index memory metasurface," *Applied Physics Letters*, 102:224103, Jun. 2013. The dissertation author was the primary investigator and author of this publication.

Chapter 4, in full, is a reprint of material as it appears in M. D. Goldflam, M. K. Liu, B. C. Chapler, H. T. Stinson, A. J. Sternbach, A. S. McLeod, J. D. Zhang,

K. Geng, M. Royal, B.-J. Kim, R. D. Averitt, N. M. Jokerst, D. R. Smith, H.-T. Kim, and D. N. Basov. "Voltage switching of a VO_2 memory metasurface using ionic gel," *Applied Physics Letters*, 105(4):041117, July 2014. The dissertation author was the primary investigator and author of this publication.

Chapter 5, in full, is a reprint of material as it appears in M. D. Goldflam, G.-X. Ni, K. W. Post, Z. Fei, Y. Yeo, J. Y. Tan, A. S. Rodin, B. C. Chapler, B. Özyilmaz, A. H. Castro Neto, M. M. Fogler, and D. N. Basov, "Tuning and Persistent Switching of Graphene Plasmons on a Ferroelectric Substrate," *Nano Letters*, vol. 15, no. 8, pp. 48594864, 2015. The dissertation author was the primary investigator and author of this publication.

Appendix A, in part, is a reprint of material as it appears in M. D. Goldflam, G.-X. Ni, K. W. Post, Z. Fei, Y. Yeo, J. Y. Tan, A. S. Rodin, B. C. Chapler, B. Özyilmaz, A. H. Castro Neto, M. M. Fogler, and D. N. Basov, "Tuning and Persistent Switching of Graphene Plasmons on a Ferroelectric Substrate," *Nano Letters*, vol. 15, no. 8, pp. 48594864, 2015. The dissertation author was the primary investigator and author of this publication.

VITA

2009	Bachelor of Science in Physics *magna cum laude*, University of California, Los Angeles
2011	Master of Science in Physics, University of California, San Diego
2015	Doctor of Philosophy in Physics, University of California, San Diego

PUBLICATIONS

M. D. Goldflam, G.-X. Ni, K. W. Post, Z. Fei, Y. Yeo, J. Y. Tan, A. S. Rodin, B. C. Chapler, B. Özyilmaz, A. H. Castro Neto, M. M. Fogler, and D. N. Basov, Tuning and Persistent Switching of Graphene Plasmons on a Ferroelectric Substrate, *Nano Letters*, vol. 15, no. 8, pp. 48594864, 2015.

S. Dai, Q. Ma, M. K. Liu, T. Andersen, Z. Fei, M. D. Goldflam, M. Wagner, K. Watanabe, T. Taniguchi, M. Thiemens, F. Keilmann, G. C. A. M. Janssen, S.-E. Zhu, P. Jarillo-Herrero, M. M. Fogler, and D. N. Basov, *Nat. Nanotechnol.* 16 (2015).

K. W. Post, Y. S. Lee, B. C. Chapler, A. A. Schafgans, M. Novak, A. A. Taskin, K. Segawa, M. D. Goldflam, H. T. Stinson, Y. Ando, and D. N. Basov, Infrared probe of the bulk insulating response in $Bi_{2-x}Sb_xTe_{3-y}Se_y$ topological insulator alloys. *Phys. Rev. B* 91, 165202 (2015).

A. S. McLeod, P. Kelly, M. D. Goldflam, Z. Gainsforth, A. J. Westphal, G. Dominguez, M. H. Thiemens, M. M. Fogler, and D. N. Basov. Model for quantitative tip-enhanced spectroscopy and the extraction of nanoscale-resolved optical constants. *Physical Review B*, 90(8):085136, Aug. 2014.

M. D. Goldflam, M. K. Liu, B. C. Chapler, H. T. Stinson, A. J. Sternbach, A. S. McLeod, J. D. Zhang, K. Geng, M. Royal, B.-J. Kim, R. D. Averitt, N. M. Jokerst, D. R. Smith, H.-T. Kim, and D. N. Basov. Voltage switching of a VO_2 memory metasurface using ionic gel. *Applied Physics Letters*, 105(4):041117, July 2014.

M. Liu, M. Wagner, J. Zhang, A. McLeod, S. Kittiwatanakul, Z. Fei, E. Abreu, M. Goldflam, A. J. Sternbach, S. Dai, K. G. West, J. Lu, S. A. Wolf, R. D. Averitt, and D. N. Basov. Symmetry breaking and geometric confinement in VO_2: Results from a three-dimensional infrared nano-imaging. *Applied Physics Letters*, 104(12):121905, Mar. 2014.

M. Wagner, Z. Fei, A. S. McLeod, A. S. Rodin, W. Bao, E. G. Iwinski, Z. Zhao, M. Goldflam, M. Liu, G. Dominguez, M. Thiemens, M. M. Fogler, A. H. Castro Neto, C. N. Lau, S. Amarie, F. Keilmann, and D. N. Basov. Ultrafast and nanoscale plasmonic phenomena in exfoliated graphene revealed by infrared pump-probe nanoscopy. *Nano letters*, 14(2):894900, Feb. 2014.

M. K. Liu, M. Wagner, E. Abreu, S. Kittiwatanakul, A. McLeod, Z. Fei, M. Goldflam, S. Dai, M. M. Fogler, J. Lu, S. A. Wolf, R. D. Averitt, and D. N. Basov. Anisotropic Electronic State via Spontaneous Phase Separation in Strained Vanadium Dioxide Films. *Physical Review Letters*, 111(9):096602, Aug. 2013.

M. D. Goldflam, T. Driscoll, D. Barnas, O. Khatib, M. Royal, N. M. Jokerst, D. R. Smith, B.-J. Kim, G. Seo, H.-T. Kim, and D. N. Basov. Two-dimensional reconfigurable gradient index memory metasurface. *Applied Physics Letters*, 102:224103, Jun. 2013.

M. D. Goldflam, T. Driscoll, B. Chapler, O. Khatib, N. Marie Jokerst, S. Palit, D. R. Smith, B.-J. Kim, G. Seo, H.-T. Kim, M. D. Ventra, and D. N. Basov. Reconfigurable gradient index using VO_2 memory metamaterials. *Applied Physics Letters*, 99(4):044103, Jul. 2011.

ABSTRACT OF THE DISSERTATION

Tuning the Optical Response of Graphene and Metamaterials

by

Michael David Goldflam

Doctor of Philosophy in Physics

University of California, San Diego, 2015

Professor Dimitri N. Basov, Chair

The following dissertation examines the tunability of two types of proof-of-concept devices centering around post-fabrication modification of the infrared optical response. The first device, created through the hybridization of the metamaterials and the phase-transition oxide vanadium dioxide (VO_2), is probed using Fourier transform infrared spectroscopy. We demonstrate that, through application of voltage pulses to this initially uniform device, a gradient in the optical properties can be obtained. This macroscopic control mechanism enables persistent modification of the device, though the hysteretic nature of the VO_2 insulator to metal transition (IMT), on spatial scales on the order of a few wavelengths of the probing light. In addition to effects from current-induced heating, we show that the optical response can also be modified through the use of an ionic gel to

oxidize or reduce the vanadium ions in VO_2, thereby driving its IMT. These measurements also demonstrate the potential for metamaterials as a means of probing metal-to-insulator transitions, allowing for enhanced optical probing of changes in VO_2 properties due to electric fields from the ion gel. The second device we explored is a graphene based device used for examining the modification of graphene's plasmonic response in conjunction with the ferroelectric high-κ dielectric lead zirconium titanate (PZT) employed as a gate dielectric. By using PZT, the carrier concentration, and therefore the optical properties of graphene, can be heavily modified with small back-gate voltages. Additionally, the use of a ferroelectric dielectric enables a form of memory in the device where transient voltage application leads to persistent changes in graphene properties. Examination of this device using scanning near-field optical microscopy allows us to determine the usefulness of similar devices in future plasmonic device.

Chapter 1

Introduction

An important aspect in the functionality of an optical device is the frequency range over which it performs its specified purpose. In the case of many optical elements including polarizers, frequency selective filters, and absorbers, this ranged is restricted. An important avenue of research in optical systems, which works to expand this range, is known as operational frequency tuning. Through post-fabrication modification of the optical response of a device, the working frequency range of devices can be broadened. Below, two methods for achieving a variable optical response are introduced.

1.1 Metamaterial tuning

1.1.1 Metamaterials

The optical response of materials is determined by the underlying atomic structure arising from the basic chemistry of the system. While a broad range of properties exist in naturally occurring materials, the ability to accurately control the optical properties of a system can lead to dramatic advances in the fucntionality of optical elements (e.g. beam-forming/steering, focusing, perfect lensing). Unlike conventional materials that have an optical response fixed by their atomic structure, metamaterials gain their optical response from engineered sub-wavelength nano-structures. It is this aspect of metamaterials that has enabled the creation

of optical responses that are impossible in nature, for example, negative index of refraction. However, such designer properties benefit greatly from post-fabrication modification. To understand one mechanism for altering the properties of a metamaterial, it is useful to examine one of the simplest metamaterials structures, the split ring resonator (SRR). An optical image of one such resonator is show in the inset of Fig 2.2. An easy way to understand this structure is to look at an SRR as a microscopic circuit composed of a resistor, inductor, and capacitor (RLC circuit). Incident light will excite current flow in the SRR. In this scenario, the gap in the ring functions as a capacitor, the ring itself as an inductor, and losses in the SRR material act as a resistor. As a result, the resonance frequency of a device composed of an array of SRRs depends directly on the inductance (L) and capacitance (C) with $\omega_{\text{res}} = \frac{1}{\sqrt{LC}}$. The capacitance of a simple parallel plate capacitor is given by

$$C = \epsilon_{\text{DC}} \frac{A}{d} \tag{1.1}$$

where ϵ_{DC} is the DC permittivity of the material in the capacitor, A is the area of the plates, and d is the distance between plates. From this relationship, it is clear that modification of ϵ_{DC} should change the metamaterial resonance without any additional fabrication. A useful means of obtaining variable ϵ_{DC} in an SRR gap is through the hybridization of phase change materials (for which ϵ_{DC} changes with applied stimulus) with metamaterial structures.

1.1.2 Vanadium dioxide

Vanadium dioxide (VO_2) has been a material of interest for decades, owing to its dramatic and not-entirely-understood insulator-to-metal transition. This transition can be triggered thermally, optically, or electrically, and has prompted intense studies ranging from transport to pump-probe optical investigations. During this transition, VO_2 undergoes a percolative change in its material properties where conductivity changes by several orders of magnitude. This conductivity change is accompanied by a divergence in its permittivity, a result of the growth and eventual joining of metallic puddles in a sample with heating. The temperature of this transition, just above room temperature (340 K), makes VO_2 an easy

material to study, eliminating the need for complex cryogenic systems. An additional useful aspect of this phase transition is that it is broadly hysteretic, as can be seen in the inset of Fig. 4.3a and b. This hysteresis enables a form of memory in VO_2 as the current resistance, within the hysteretic region, depends not only on the current temperature, but also on previous temperatures. These characeristics position VO_2 as an ideal candidate for creation of tunable metamaterials. One of the simplest means of modifying the properties of VO_2 is through the use of an ionic liquid or gel. These gels contain many mobile ions (both positive and negative) and enable formation an electric double layer at the surface of a sample. This layer, effectively a nanometer wide capacitor, generates very large electric fields with only small applied voltages. These fields are able to oxidize or reduce vanadium ions in VO_2 thereby electrochemically promoting a change in conductivity. While electrochemical modification occurs on timescales longer than those possible thermally or optically, these changes can occur at temperatures below the thermally activated transition, making ion gel gating an intriguing alternative to heating.

1.1.3 Hybridized metamaterial structures

As described above, through the combination of metamaterials with phase change materials like VO_2, a form of dynamic optical response can be achieved. While homogeneous tuning of a device provides significant benefits over a fixed optical response, further usefulness can be obtained through position dependent modification of a metasurface. In Chapter 2, we demonstrate tuning of a metamaterial device that incorporates a form of spatial gradient control. Electrical tuning of the metamaterial is achieved through a vanadium dioxide layer which interacts with an array of split ring resonators. We achieved a spatial gradient in the magnitude of permittivity, writeable using a single transient electrical pulse. This induced gradient in our device is observed on spatial scales on the order of one wavelength at 1 THz. Additionally, in Chapter 3, we show that through modification of the spatial and temporal distribution of current, we can obtain increased control over the shape of these gradients. We are able to write spatially sharp

gradients with a ∼50% change in the index of refraction over length scales of only a few wavelengths as observed through diffraction limited terahertz spectroscopy. Furthermore, we assess the potentials for such gradients for beam-steering applications.

While electrical tuning of such devices is one avenue of control, alternative control schemes exist, for example, through ion gel usage. In Chapter 4 we demonstrate an electrolyte-based voltage tunable VO_2 memory metasurface. Large spatial scale, low voltage, non-volatile switching of terahertz (THz) metasurface resonances is achieved through voltage application using an ionic gel to drive the insulator-to-metal transition in an underlying VO_2 layer. Positive and negative voltage application can selectively tune the metasurface resonance into the off or on state by pushing the VO_2 into a more conductive or insulating regime respectively. Compared to graphene based control devices, the relatively long saturation time of resonance modification in VO_2 based devices suggests that this voltage-induced switching originates primarily from electrochemical effects related to oxygen migration across the electrolyte-VO_2 interface. The techniques discussed in Chapters 2 and 3 point towards a macroscopic tuning mechanism for metamaterials that shows decreased complexity, in comparison to addressing individual units celts. Additionally, the memory present in such devices obviates the need for continuous stimulation.

1.2 Graphene plasmonics and near-field microscopy

1.2.1 Graphene

With the experimental discovery of single layer graphene in 2003 by Andre Geim and Konstantin Novoselov, came a flurry of research into its unique and exciting material and electronic properties. This hexagonal lattice of carbon atoms possesses exemplary optical and mechanical response including excellent thermal and electrical conductivity, very high tensile strength, and an easily tunable opti-

cal response. Graphene, like many metals, supports propagating surface plasmons: charge density waves moving at the interface of graphene and dielectric materials. In contrast to nobel metals, graphene's plasmonic response is easily and broadly tunable through back-gating, making graphene a viable material for plasmonic applications from terahertz to mid-infrared frequencies. Back-gating involves placing graphene in a capacitor-like layered structure with a graphene flake layered on a gate dielectric, followed by a metallic layer (known as the back-gate). Through application of a voltage between the graphene and the back-gate, the carrier concentration of graphene can be conveniently modified. With an applied voltage, V, the modification of the carrier concentration, n, in graphene is given by:

$$n = \frac{\epsilon_{DC}|V_G - V_{\mathrm{CNP}}|}{ed} \tag{1.2}$$

where ϵ_{DC} is the dielectric constant of the gate dielectric, V_G is the voltage applied between graphene and the back-gate, V_{CNP} is the voltage of the charge neutrality point of graphene, e is the electron charge, and d is the thickness of the gate dielectric. The strength of this tuning, as well as the overall properties of graphene, are heaving dependent on its surrounding dielectric environment. As a result, it is important to examine the a range of dielectrics as substrates for graphene.

1.2.2 Scattering-type scanning near field optical microscopy and plasmon imaging

While far-field infrared spectroscopy is capable of extracting information on a wide range of phenomena (e.g. phonons and excitons), it suffers from physical laws that limit the probing area size, providing only area averaged results. The diffraction-governed limit prevents examination of features that occur on length scales smaller than about half the probing wavelength, determined by limitations on far-field optics. The demonstration of scanning near field optical microscopy (SNOM) has enabled significant advances in infrared optics allowing for real space imaging of sub-diffraction limited sample variation. The aperture-free operation mode of this technique integrates conventional infrared optics with an atomic force microscope (AFM). Importantly, this integration enables simultaneous topographic

and optical measurements of a sample allowing for correlation of features measured by these two independent measurements. Focusing of an infrared beam on a metallic AFM tip causes sub-wavelength confinement of the beam at length-scales determined by the tip radius, a result of evanescent fields excited by the tip, which for commercially available tips is ∼20 nm. This combination means that for infrared wavelengths on the order of 10 μm, the sample is probed at length-scales several hundreds of times smaller than those afforded by diffraction limited optics. In general, the wavelength of plasmons in graphene, for excitation frequencies $\omega \sim 1000$ cm^{-1}, are on the order of several hundred nanometers, nearly two orders of magnitude less than those of light of that frequency propagating in free space. As a result, for a given frequency, the momentum of a plasmon is significantly larger than what is provided by free space light. This points to a second benefit of SNOM over far field techniques for examination of surface plasmons. In addition to the focusing benefits provided by the confined light, the evanescent fields discussed above also provide significantly more momentum to the system being probed. It is this momentum that makes near-field microscopy capable of launching and detecting propagating polaritonic waves as shown schematically in Fig 1.1.

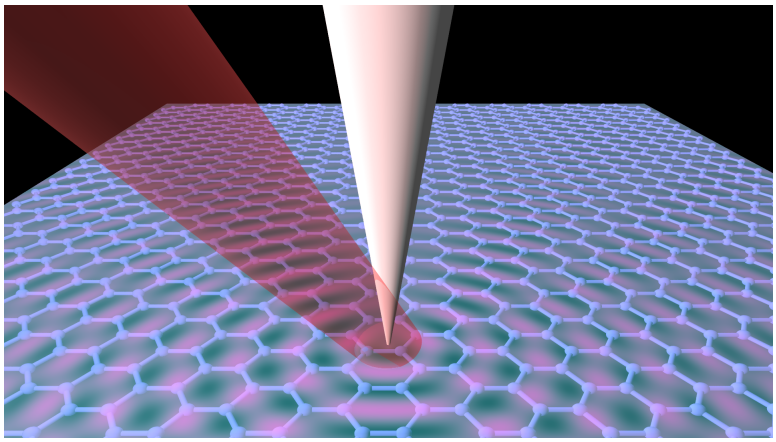

Figure 1.1: Schematic representation of a near field experiment. Infrared light (red) is incident on the AFM tip (white cone) in close proximity to graphene lattice launching radially propagating plasmonic waves.

In Chapter 5, we employ SMOM to examine the propagation of plasmons in

graphene on thin films of the the high-κ dielectric $PbZr_{0.3}Ti_{0.7}O_3$ (PZT). Significant modulation (up to $\pm 75\%$) of the plasmon wavelength was achieved with application of ultrasmall voltages ($< \pm 1$ V) across PZT. Analysis of the observed plasmonic fringes at the graphene edge indicates that carriers in graphene on PZT behave as noninteracting Dirac Fermions approximated by a semiclassical Drude response, which may be attributed to strong dielectric screening at the graphene/PZT interface. Additionally, significant plasmon scattering occurs at the grain boundaries of PZT from topographic and/or polarization induced graphene conductivity variation in the interior of graphene, reducing the overall plasmon propagation length. Lastly, through application of 2 V across PZT, we demonstrate the capability to persistently modify the plasmonic response of graphene through transient voltage application.

Previous real space measurements of backgated graphene plasmons have focused on conventional graphene substrates (e.g. SiO_2, hBN, SiC). However, as demonstrated in this chapter, use of ferroelectrics with high dielectric constants, such as PZT, may allow for more practical plasmonic devices with high efficiency plasmon tuning and the added potential for polarization-driven memory-enabled tuning of graphene plasmons. While previous works on graphene/ferroelectric devices focused primarily on graphene's electronic properties, this research is the first to focus on its plasmonic and photonic characteristics.

Chapter 2

Reconfigurable Gradient Index using VO_2 Memory Metamaterials

2.1 Introduction

Metamaterials have progressed from academic curiosities [1, 2] to candidates for real-world applications. Emerging metamaterial applications range from radio frequency (RF) [3] communications to millimeter radar [4]. One key technique which promises to further the applicability of metamaterials is tunability. Operational frequency tuning has been presented as one solution to the narrow bandwidth often present in metamaterial devices [5, 6]. Frequency-agile metamaterial designs have been demonstrated across a wide spectrum from microwave [7] to near-visible frequencies [8].

To date, tuning has generally been homogeneously implemented across the entire device as a whole. Developing techniques for controllable spatially variable tuning will present the possibility of devices with a reconfigurable gradient index of refraction (GRIN). GRIN devices have already proven an attractive area for metamaterials [9], as the metamaterial design process naturally allows for the control needed to fabricate GRIN structures. Additionally, use of spatially nonuniform tuning can leverage the narrow bandwidth of metamaterials in a unique way. For narrow-band operation, minor adjustments in the resonance frequency of a meta-

material can translate to large changes in the index of refraction at that frequency. Overall, spatial control of resonance tuning allows for post-fabrication modification of the index of refraction and therefore the creation of a reconfigurable gradient.

We demonstrate a spatially reconfigurable THz hybrid metamaterial with vanadium dioxide (VO_2) and split ring resonators (SRRs) as constituent elements. The SRR has been the "fruit fly" of metamaterials research, allowing for convenient implementation of optical characteristics which are unattainable without metamaterials [1, 10, 11]. Our device is composed of an array of 100 nm thick gold SRRs (dimensions shown in figure 2.2) lithographically fabricated on 90 nm thick VO_2 grown on a sapphire substrate. VO_2 undergoes an insulator to metal transition [12] which can be triggered thermally electrically [13] or optically [14]. The phase transition is hysteretic, and therefore, changes in the conductivity of VO_2 generally persist, provided the device temperature is maintained. Hybrid metamaterial-VO_2 devices benefit from this memory [15], and from the large tuning dynamic range achievable with VO_2. Persistent tuning uses this memory to eliminate the need for continuous stimulation or repeated excitation of the device. Our measurements demonstrate the ability to perform persistent tuning of a hybrid SRR-VO_2 device with a spatial configuration, writing a gradient in the permittivity of the hybrid metamaterial.

2.2 Experimental details

To interrogate our metamaterial, we performed infrared transmission spectroscopy using a home-built broadband IR microscope. Linearly polarized light from a mercury lamp was focused via reflecting optics to a normally-incident spot $\sim$100μm in diameter. In far-infrared, this spot facilitates nearly diffraction-limited measurements of the metamaterial local response. The sample was mounted on a translator allowing for linear movement across the entire device. Integration of a temperature stage with proportional-integral-derivative controller (PID) feedback allowed us to control device temperature to better than $\pm$0.05 K. For these experiments, we kept the device at a constant temperature of 339.5 K (just below

the temperature of the insulator-metal transition in VO_2) to allow for maximal transition during the voltage application discussed below.

2.3 Results

2.3.1 Calibration spectra

Prior to the application of any current pulse, calibration transmission spectra were collected at positions across the sample at 339.5 K. In these spectra, the peak position of 1-$T(\omega)$ (transmission) indicates the resonance frequency of the hybrid metamaterial. In our setup, the device was oriented to electrically excite the lowest order RLC-oscillation mode of the SRR. The increasing permittivity of VO_2 as its phase transition progresses increases the capacitance of each SRR. This in turn reduces the effective time constant of the RLC-oscillation mode thereby decreasing the resonance frequency of the hybrid SRR-VO_2 device. Additionally, losses in the metallic regions of VO_2 cause damping of the resonance. These calibration spectra are nearly identical with uniform resonance positions, indicating the homogeneous (on a mesoscopic effective medium scale) initial state of our device.

2.3.2 Current induced gradient index creation

To electrically write a spatial gradient to the device, we applied a square voltage pulse of 175 V $\times$ 2.5 s across the contact points as shown in Fig. 2.1 (top inset). This voltage pulse did not significantly affect average temperature of the device as the total input energy is small compared to the thermal inertia of the sapphire substrate. However, as current flowed almost exclusively through the VO_2-SRR layer, local transient heating of this layer occurred. While the dominant switching mechanism in this device is thermal, there may be additional electrical switching from the applied voltage. Inquiry into the microscopic mechanisms of switching is an active area of VO_2 research [13, 14] but is beyond the scope of our work, which focuses on the utility and applications of switching effects. As VO_2

undergoes its transition from insulator to metal [16], we expect the peak of the resonance to redshift and become damped [17]. Such transient heating leaves a persistent change due to the hysteresis in VO_2 [15, 17].

The placement of electrical contacts was designed to induce a gradient in the current density passing through the VO_2-SRR layer. Using our translation stage, we probed 8 locations on the sample, ranging from directly between the contacts (0 mm) to +3.5 mm above the contact path as shown in Fig. 2.1 (top inset). In Fig. 2.1, we plot transmission spectra at these 8 positions. The redshift of the absorption resonance is more prominent for positions in close proximity to the contacts. This is consistent with the idea that the percolative phase transition in VO_2 has progressed further near the contacts. The maximum resonance redshift is about 10% of the center frequency, and nearly 50% of that obtained from the entire insulator-metal transition [17]. Through a comparison of the measured resonance frequencies to those in a previous work using the same device [17], we estimated an effective temperature gradient, during and shortly after the current pulse, ranging from ∼342 K at 0 mm, to ∼340 K at 3.5 mm. Additionally, this experiment demonstrates that metamaterials can be probed and meaningfully modified on spatial scales on the order of a wavelength. The total spatial extent of our observed gradient is 3.5 mm, with 8 data points over this distance. Thus, these distinct spectra are recorded with a spacing of just under 1.5λ ($\lambda = 300$ μm at 1 THz).

2.3.3 Optical property extraction

To better quantify the potential of such gradients, we retrieved the optical parameters from the transmission curves by fitting. Permittivity gives a better visualization of the gradient in material response than transmission, especially in a single-layer metamaterial where overall transmission is generally high. The retrieval procedure is a two-oscillator fitting using Lorentzian oscillators $\bar{\epsilon}$ and $\bar{\mu}$ weighted by spatial-dispersion cofactors [18,19] to give a close approximation to the homogenized effective permittivity, ϵ_{eff}, and permeability, μ_{eff} of the metamaterial layer:

$$\epsilon_{\text{eff}} = \bar{\epsilon}\frac{(\theta/2)}{\sin(\theta/2)}\left[\cos(\theta/2)\right]^{-S_b} \tag{2.1}$$

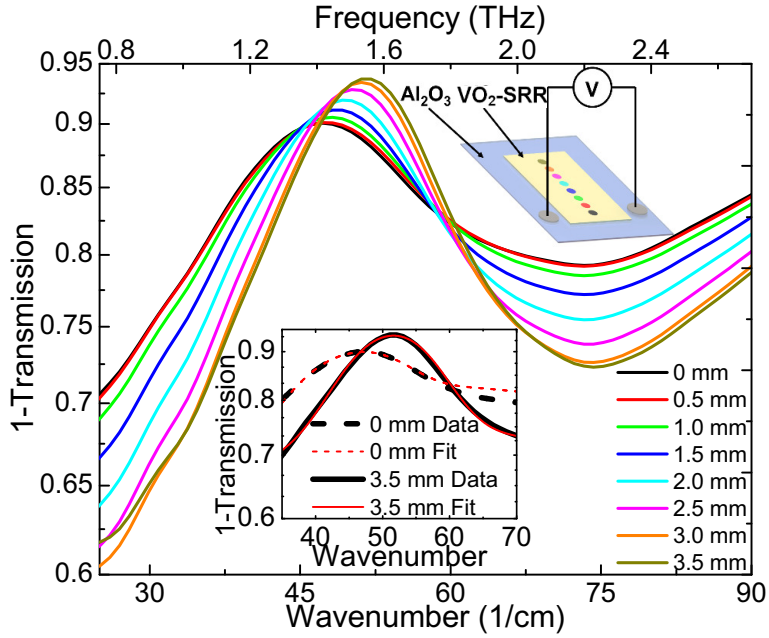

Figure 2.1: Transmission measurements taken along the hybrid metamaterial at 339.5 K. 0 mm indicates a position midway between the contacts. (Bottom inset) Measured transmission curves along with fits. (Top inset) Schematic of device indicating contact geometry and measurement locations.

$$\mu_{\text{eff}} = \bar{\mu}\frac{(\theta/2)}{\sin(\theta/2)}\left[\cos(\theta/2)\right]^{S_b} \tag{2.2}$$

where θ is the phase advance across one cell, and $S_b = 1$ for electric resonators or $S_b = -1$ for magnetic resonators. The resonance frequency, strength, and damping constant of the two oscillators [20] underlying the effective optical parameters were modified to obtain good agreement between measured and fitted spectra. While better agreement may have been obtained through the use of a large number of oscillators, this procedure increases numerical complexity, and can often obscure insight into the underlying physical processes involved in the material response, here the magnetic (ω_0) and electric (ω_1) modes of the SRR [21]. These oscillator parameters were then used to determine permittivity and permeability of our device. Resultant fits for the most shifted (0 mm) and least shifted (3.5 mm) transmission spectra are shown in Fig. 2.1 (bottom inset). The fits capture the most prominent features of the transmission spectra. They also model the pulse-induced redshift and damping of the resonance.

The real and imaginary permittivity extracted from these fits are shown in Fig. 2.2. These figures illustrate the range of complex permittivity values simultaneously present at different locations in the device. By interpolating between the 8 points where the spectra were obtained, we extracted a spatial map of the metamaterial permittivity response, shown in Fig. 2.3a. At locations nearer to the contacts, the resonance becomes increasingly redshifted due to the increasing number and density of metallic puddles in VO_2. The overall frequency tuning range of our device compares favorably with many techniques for frequency-agile metamaterials [17,22]. At the initial resonance frequency (∼1.23 THz), the overall percent change in real permittivity is 70% across the sample, enough to satisfy many potential GRIN device applications.

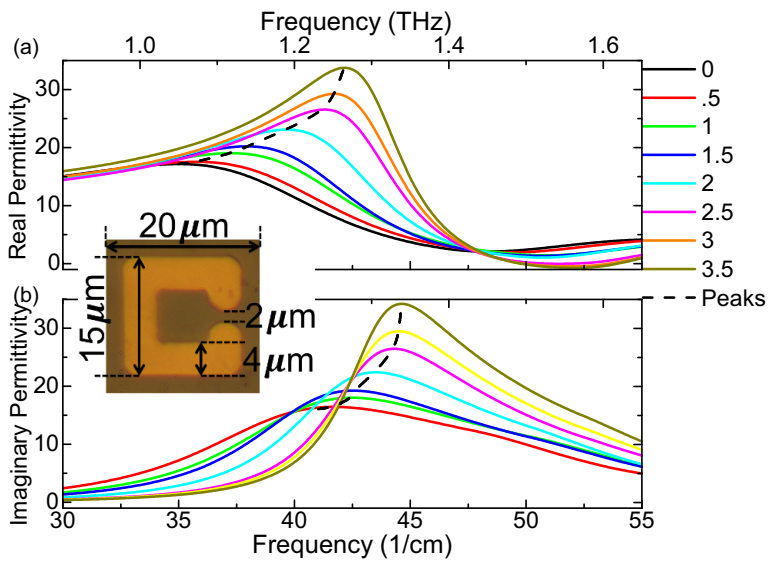

Figure 2.2: Extracted values for real (a) and imaginary (b) permittivity. Position of maximum permittivity indicated by dashed lines. (Inset) Schematic of SRR unit cell.

2.3.4 Understanding gradient creation through variable current density

The shift in resonance position in our transmission spectra is a result of the application of a transient voltage pulse as described previously. Current flowing

through the device heats the VO_2 with power dissipated given as $P = I^2R$. We expect that areas of the device nearer to the contacts were exposed to a larger current density, and as a result the VO_2 will have progressed through a greater amount of its phase transition. To model this situation, we performed a simulation of current flow and power dissipation in our device using COMSOL, a finite element simulation program. The results of this simulation are shown in Fig. 2.3b. As expected, the greatest power dissipation occurs in areas near the contacts. These results fit with our picture of a spatial gradient of permittivity induced by inhomogeneous excitation of the VO_2 phase transition.

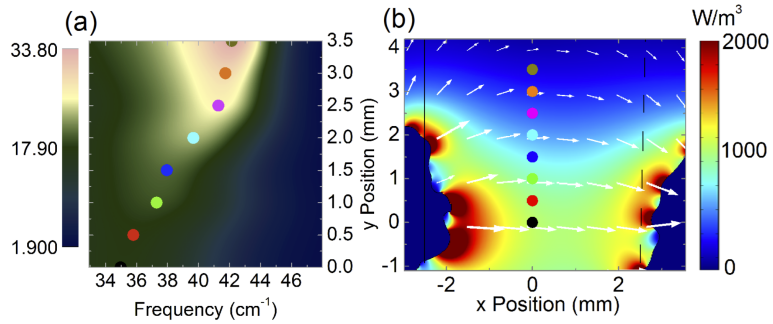

Figure 2.3: a) Spatial map of real permittivity varying with vertical position and frequency. Resonance frequency locations indicated by colored points. b) Simulation of current flow through device. Color indicates power density (W/m^3) and current flow is shown in the vector field (A/m^2). Black rectangular outline indicates the location of the SRR array and VO_2. Contact locations and shapes indicated by outlines at the bottom of the device.

2.4 Conclusions

Our SRR-VO_2 device is the simplest hybrid metamaterial structure with which to explore advantages of spatial gradient tuning. With it, we have shown the ability to induce and spectroscopically probe a persistent spatial gradient within a previously uniform device. Use of finer, or even pixel-by-pixel, control over switching would allow for creation of more precise gradients. Such pixel-level switching nearly necessitates the existence of memory within the device as the difficulty of

repeated or sustained excitation would make detailed switching unfeasible. Future flexibility in the optical parameters of metamaterials as a result of tuning occurring on the pixel level will enable the creation of dynamic hybrid metamaterial structures suitable for a wide range of applications.

2.5 Acknowledgements

Chapter 2, in full, is a reprint of material as it appears in M. D. Goldflam, T. Driscoll, B. Chapler, O. Khatib, N. Marie Jokerst, S. Palit, D. R. Smith, B.-J. Kim, G. Seo, H.-T. Kim, M. D. Ventra, and D. N. Basov. "Reconfigurable gradient index using VO_2 memory metamaterials," *Applied Physics Letters*, 99(4):044103, Jul. 2011. The dissertation author was the primary investigator and author of this publication.

The authors wish to acknowledge the funding for this project from AFOSR and the creative research project of ETRI.

Chapter 3

Two-dimensional reconfigurable gradient index memory metasurface

3.1 Introduction

Metamaterials have allowed for the creation of materials with novel properties, such as negative index [1, 23], however, it is fine control over gradients in the index of refraction (GRIN), impedance, and absorption that have yielded some of the first applications. Static gradients, engineered into the fixed initial design of a device, have been demonstrated yielding beam-steering and beam-focusing metamaterial lenses [9, 24–26] as well as metasurfaces for coupling of propagating waves into surface waves [27]. While the functionality of these devices is limited due to their static nature, through integration of tunability, it is possible to improve on the capabilities of such devices by modification of their gradients after device fabrication.

Tunability has been previously demonstrated in metamaterials. Application of an external electric field has enabled modification of metamaterials on unit cell length scales, however, this level of control greatly increases complexity in real-world devices due to independent wiring of individual cells and the need for

continuous field application [28–30]. One mechanism for circumventing this need for continuous stimulation is through the integration of a form of memory into each unit cell. Such memory can be achieved by creating a hybrid metamaterial formed through the combination of standard metamaterial elements with naturally hysteretic materials such as phase change materials, ferromagnetic materials, or materials that exhibit Kerr-type nonlinearity [15, 17, 31, 32]. This form of hybridization enables tuning to persist following the removal of the stimulus.

We use such a memory hybrid metamaterial to demonstrate detailed control over a persistent two-dimensional reconfigurable gradient index metasurface. Our hybrid device consists of gold split ring resonators (SRR) designed with a resonance at $\sim$55 cm^{-1} shown in the inset of Fig. 3.3, which are lithographically fabricated on a 90 nm thick layer of vanadium dioxide (VO_2). The use of VO_2 in the device allows for memory-enabled tuning of the device optical properties achieved through the hysteretic insulator-to-metal phase transition (IMT) of VO_2, as has been previously investigated [13, 14, 17, 33–35]. While previous work has focused primarily on the underlying physics of VO_2 and the memory effects made possible through its use, in this work we focus on the detailed control we can obtain using a VO_2-hybrid memory metamaterial. While exact control can be obtained through wiring of each unit cell [36], this increases the complexity of tuning. Rather than employing this method, we devised a more practical mechanism for simultaneous modification of the entire device based on the spatial and temporal shaping of electrical current stimulation.

This simplified tuning method employs voltage pulses to modify the properties of our device. The resulting current from these voltage pulses flows primarily within the VO_2 layer. The power dissipated in a given region of the device is proportional to the square of the current in that region ($P = I^2R$). The resulting properties of each region depend on the maximum temperature reached in that region. Therefore, through control of the current duration and distribution, it is possible to control the final properties of the device. While the primary cause of shifts in VO_2 properties is resistive heating, the electric field from voltage application may play a role as well [13]. Spatial shaping of current flow is obtained

through engineering of contact geometry. Our contacts are designed to allow for control of current within each quarter of the device and consist of a semicircular arc divided into four segments, as well as a small circular disk at the center of this arc as shown in the inset of Fig. 3.1. While these pulses last for only a few seconds, the shifts in the VO_2 material properties are persistent due to the hysteretic nature of the IMT [8, 17]. The resulting increases in permittivity and conductivity of the thin film during the IMT cause a redshift in the device resonance frequency as well as a damping of the resonance, respectively [15].

3.2 Experimental details

To interrogate our device, we employed a Bruker Fourier transform infrared spectrometer with the sample placed at the focus of a mirror-based beam condenser. A two-dimensional scanning stage was constructed to allow for automated translation of our sample through this focus. This allows us to image our device on nearly diffraction limited length scales on the order of 0.01 mm^2. The sample was mounted on the translation stage allowing for measurements throughout the full area of the device. Use of a temperature stage allowed for control of the device temperature to within ± 0.05 K. Throughout these measurements, our device was kept at a uniform average temperature of 339.9 K, the temperature of the steepest part of the VO_2 transition. This maximizes the effects of heating from the voltage pulses described in the following paragraph.

3.3 Current flow control using contact geometry

Precise control of gradients in our device requires restriction of current flow to desired areas. To select which region of the device experiences the greatest heating, resistors of varying values were placed in series with each of the outer contacts. The greatest current flows through the contact with the smallest attached resistor. Additionally, these resistors serve to regulate overall current flow and prevent run-away heating as the VO_2 becomes increasingly metallic. A second

mechanism for controlling the created gradients is modification of pulse duration and strength. Through application of multiple weaker pulses, it is possible to confine heating more tightly than through one strong pulse. With a single large pulse, we run the risk of heating the device beyond the hysteretic region of the VO_2 transition, preventing the creation of a gradient. By applying several shorter pulses, we are able to more carefully control the overall heating of the device. Each successive pulse enhances and reinforces the gradient established by the previous pulses, as the largest current will flow in the areas which have already undergone the greatest heating and therefore have the lowest resistance.

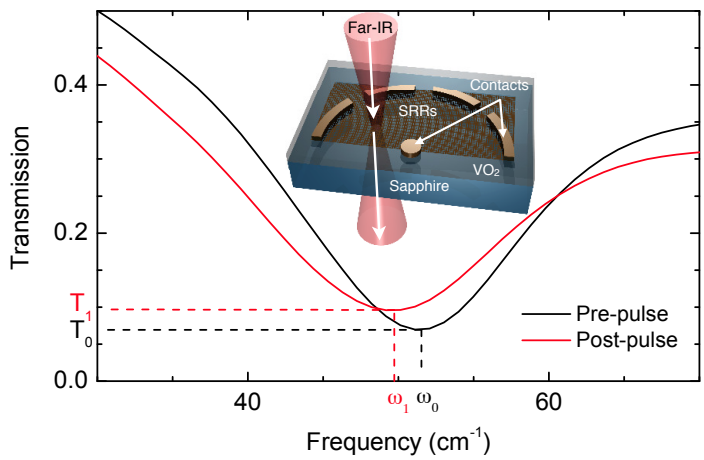

Figure 3.1: Pre-pulse (black) and post-pulse (red) unprocessed spectra for transmission at one position on the device. Schematic showing normalization method for transmission maps in Fig. 3.2. Normalized transmission is given by $T_{\text{norm}} = T_1 - T_0$ which is calculated independently for each measurement location. (Inset) Schematic of hybrid device showing contact locations and shapes as well as far-infrared light for transmission.

To cancel out any pre-existing gradients resulting from variation in SRR shape during fabrication, we normalized our spectra to pre-pulse spectra at each pixel as shown in Fig. 3.1. These normalized spectra indicate variation in the optical properties of our device due only to pulse application with larger values of T_{norm} indicating more heating and greater shifts in the resonance frequency of the device. The spectra shown in Fig. 3.1 are characteristic for pre- and post-pulse spectra at a given location and averaged over a diffraction limited spot.

3.4 Results

3.4.1 Gradients in device transmission

The resulting gradients in T_{norm} from pulse application for the various resistor setups and pulses are shown in Fig. 3.2. These plots demonstrate the ability to control which regions of the device are heated thereby enabling the creation of specific gradients within the device. The strength and breadth of the gradient can be designed and the location of the regions which reach the highest temperature during pulsing can be chosen through resistor selection. Additionally, there is an observed tradeoff between localization of current density and the strength of the gradient as can be seen through a comparison of Figs. 3.2a and 3.2c. The large shifts in optical properties across the device seen in Fig. 3.2a come with the consequence of heating a greater fraction of the SRR array while the strong confinement of heating in Fig. 3.2c shows a smaller shift in the properties from their initial pre-pulse values. The maximum shift in the resonance frequency as a result of pulsing is 7 cm^{-1}, 14% of the unshifted resonance frequency at 339.9 K. This shift in resonance frequency corresponds to a maximum change in transmission of 60% of its value at the resonance frequency, with the largest shifts seen in Fig. 3.2a. Our macroscopic control mechanism allows for modification of optical properties on spatial scales on the order of tens of unit cells (several hundred micrometers).

3.4.2 Simulations

To examine the suitability of such devices for applications, we performed simulations using ANSYS HFSS to extract the optical properties of such an SRR array. These simulations were performed for VO_2 conductivity and permittivity values corresponding to temperatures ranging from 340 K to 343 K in 1 K increments [14], the range of our effective temperature gradient as a result of the voltage pulse. This effective temperature range is obtained through a comparison of post-pulse spectra to spectra taken while uniformly heating the device. The resulting indicies of refraction and absorption coefficients for these simulations are shown in Fig. 3.3. This plot shows the range of accessible indices of refraction

available through our tuning method.

3.5 Exploration of applications

3.5.1 Beam deflection

In determining the potential for applications of such hybrid metamaterials, it is helpful to examine the capabilities of the gradients we create as applied to previously investigated GRIN architectures. One such architecture is beam deflection through the use of several identical metamaterial arrays placed in succession within a waveguide cavity. For such a geometry, the deflection angle θ is given by [25]

$$\sin\theta = \frac{N_z a_z \Delta n}{a_x} \tag{3.1}$$

where N_z is the number of unit cells along the propagation direction (z-axis), Δn is the difference in index of refraction between adjacent cells along the x-axis with the cells along the y-axis being identical to their neighbors, and a_x and a_z are the distances between units cells along the x and z-axes respectively. Based on our measurements and simulations, the maximum variation in the index of refraction in our device is 2 and occurs at a frequency of 45 cm^{-1} over a distance of 3.5 mm (175 unit cells). With 10 arrays in series, these parameters yield a maximum deflection angle of 6°, which has been previously demonstrated using fixed GRIN metamaterial arrays [25]. However, unlike the previously demonstrated devices, the gradient within our device is rewritable which would confer the ability to change this deflection angle through modification of successive arrays.

3.5.2 Beam-steering by phase discontinuities

An alternative beam-steering mechanism exploits manufactured phase discontinuities [37]. The existence of such a discontinuity allows for control of the refraction angle for transmitted light across this boundary. In such a scenario, the angle of refraction for normal incidence is given by

$$\sin(\theta_t) = \frac{\lambda_0}{2\pi n_t}\frac{d\Phi}{dx} \tag{3.2}$$

where λ_0 is the incident wavelength, n_t is the index of refraction of the material being transmitted into, and $\frac{d\Phi}{dx}$ gives the change in the phase along the boundary. From transmission simulations, we have determined that the phase gradient across our device, given our existing effective temperature gradients, is 0.7 rad/m yielding an angle of refraction of only 1°. However, in this scenario it is important to note that our device was designed with a resonance frequency ∼55 cm^{-1}. It would be feasible to increase the size of the SRRs and decrease the resonance frequency of our device while maintaining the same gradient spatial scales. The primary limit to our spatial scales is electrical current confinement within our device which remains constant regardless of overall device size. By increasing unit cell size, it would be possible to increase the refractive angle of such a device while maintaining the same tuning method.

3.6 Conclusions

Our tuning mechanism demonstrates a method for dramatically decreased complexity in optical parameter modification in metamaterials in comparison to control-line tunable metamaterials. The inclusion of memory in metamaterials further alleviates some of the difficulty resulting from continuous stimulation. It presents an alternative path to tuning where continuous stimulation may be difficult, for example when tuning through stress and strain or though applied magnetic field. Tradeoffs exist between the complexity of gradients and practicality of tuning. However, for a variety of applications [25], the level of control we attain may be all that is necessary to allow for use of such tunable hybrid metamaterials.

3.7 Acknowledgements

Chapter 3, in full, is a reprint of material as it appears in M. D. Goldflam, T. Driscoll, D. Barnas, O. Khatib, M. Royal, N. M. Jokerst, D. R. Smith, B.-J. Kim, G. Seo, H.-T. Kim, and D. N. Basov. "Two-dimensional reconfigurable gradient index memory metasurface," *Applied Physics Letters*, 102:224103, Jun. 2013. The

dissertation author was the primary investigator and author of this publication.

The authors wish to acknowledge funding for this project from AFOSR and the creative research project of ETRI.

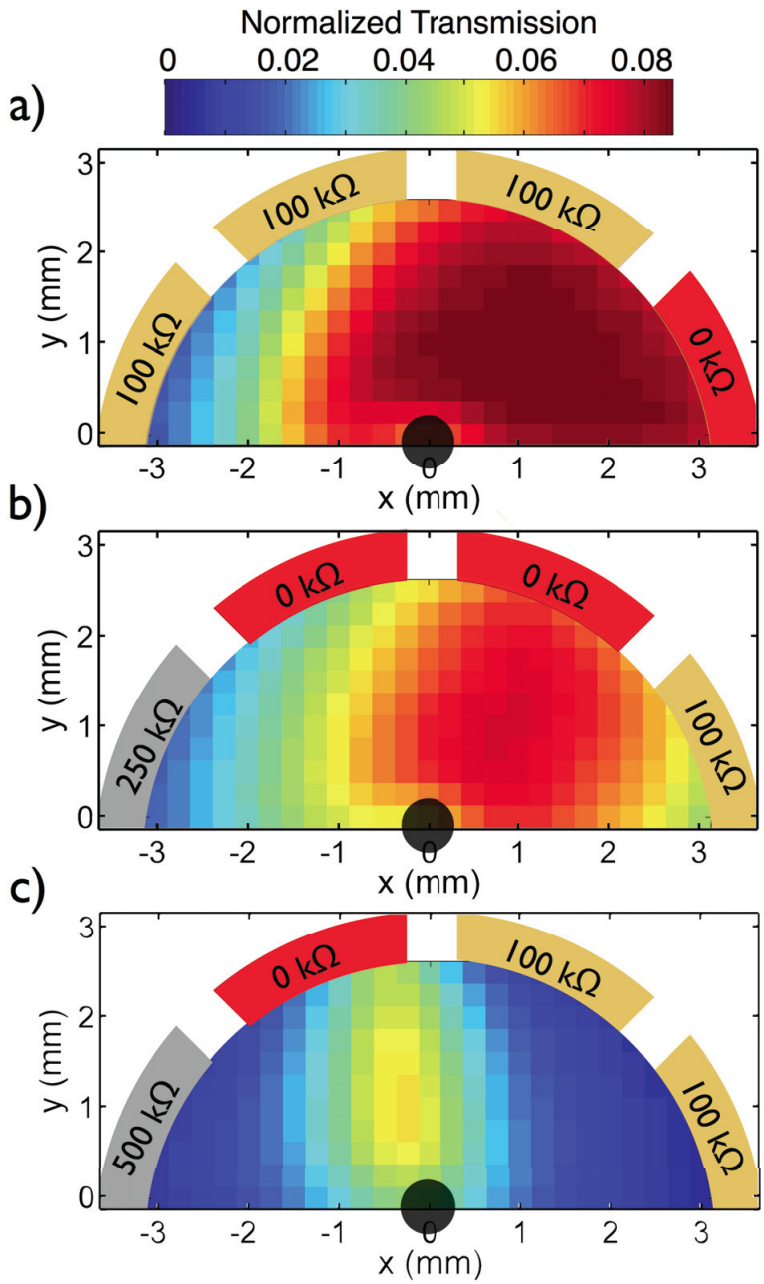

Figure 3.2: Plots of transmission at the resonance frequency for each position within the sample after application of voltage pulses. Each pixel in the plots represents the results of a spectrum at a single measurement location. Results are interpolated near the contacts. Hotter colors indicate a greater shift in the transmission at resonance. Contact locations are indicated by red, yellow and gray outlines roughly corresponding to the current strength (resistor size) in that region. a) Application of one 140 V×1.5 s followed by two 125 V×1.5 s pulses. b) Application of four 150 V×1.5 s pulses. c) Application of four 115 V×1.5 s pulses.

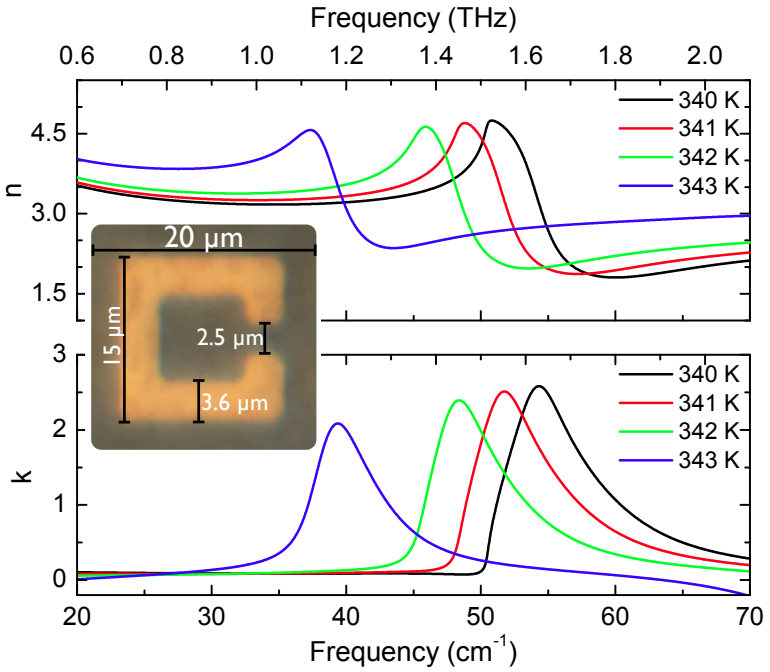

Figure 3.3: Index of refraction and absorption coefficient of our device obtained from HFSS simulations. (Inset) Schematic of unit cell of our device with dimensions.

Chapter 4

Voltage switching of a VO_2 memory metasurface using ionic gel

4.1 Introduction

In strongly correlated electron materials, competing spin, orbital, and lattice interactions result in complex phase diagrams. This complexity enables wide tunability of material properties in response to relatively weak external stimuli. A potent example is the direct modification of carrier density and orbital occupancy [38, 39] of complex materials via the electric field effect [28, 40]. Among the various electric field effect techniques, electrolyte gating has created enormous interest due to its potential for high sheet-carrier-densities [41, 42]. For example, it has been shown that in $NdNiO_3$ [43], $LaCaMnO_3$ [44], $SrTiO_3$ [45], and superconductors [46], electrostatic modification through electrolyte gating allows for tuning of the conductivity as well as the insulator-to-metal, magnetic, and/or superconducting phase transition temperatures [45].

However, voltage-induced switching is not restricted to electrostatic tuning but can also stem from electrochemical modification. Electrochemical effects have already been explored and exploited by the microelectronics community [47, 48].

For example, switchable semiconductors such as WO_x [49], TaO_x [50], and TiO_x [51] have created a new generation of resistive memory (ReRAM) devices that may emerge as alternatives to silicon-based integrated circuit technology. While the condensed matter community has extensively researched the clean physics of intrinsic electrostatic doping [52], electrochemical sample modification has found its own place in electric field controlled nonvolatile switching applications [53].

4.2 Experimental details

4.2.1 Devices

We report on electrolyte-enabled experiments using two different THz photonic devices: (1) an array of split ring resonators (SRR) covered with a single layer of graphene grown using chemical vapor deposition (CVD) shown in the inset of Fig. 4.2a, (2) the VO_2 hybrid metasurface shown in the inset of Fig. 4.2b. We found that electrolyte gating can be used to control the resonant response of both of these devices. Specifically, we were able to achieve reproducible and reversible ambipolar modification of each devices THz optical response.

4.2.2 Ion gels

We make our THz transmissive ion gel by mixing ionic liquid EMIM-TFSI with copolymer P(VDF-HFP) with a weight ratio of 1:4, following Ref. [41]. We apply a $\sim$50 μm thick layer of ion gel to our devices as illustrated in Fig. 4.1. This thin ion gel has minimal THz absorption and is, therefore, ideal for long wavelength transmission measurements [54–56]. Transmission through this film is nearly temperature independent in our investigation varying by less than 2%. Each device is probed using THz time domain spectroscopy and is placed in high vacuum prior to voltage application. The switchable area of these devices is approximately 10×5 mm^2,which is sufficient for most THz-based applications.

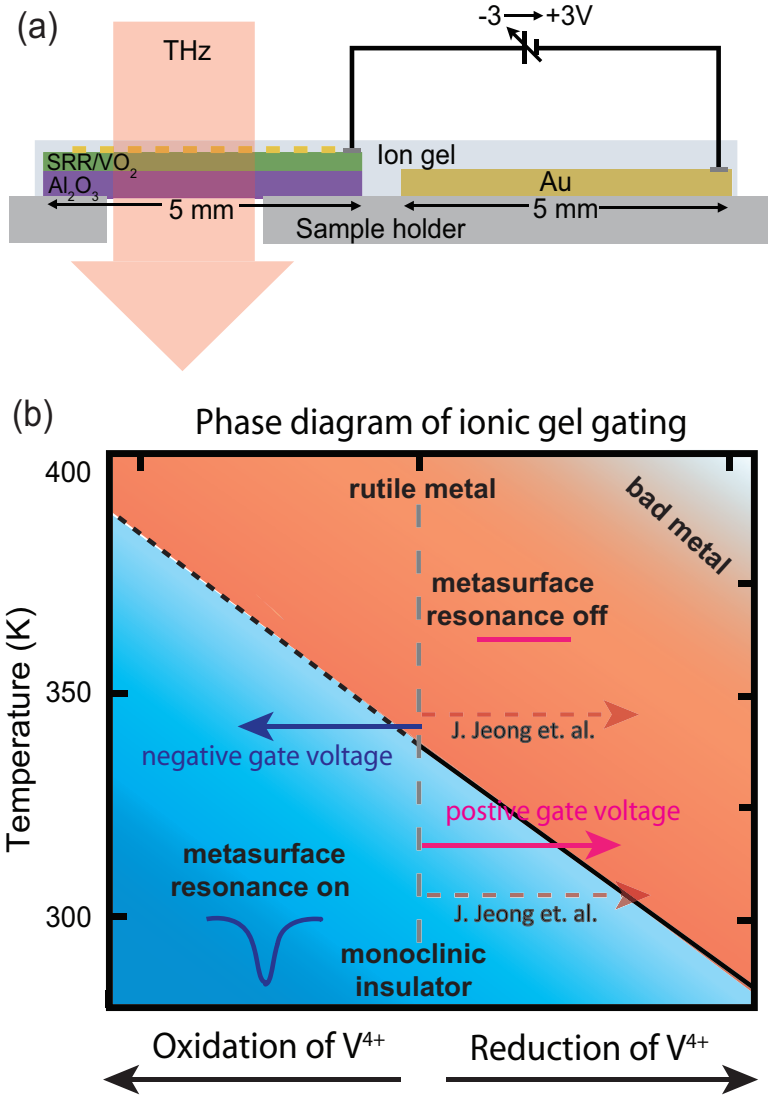

Figure 4.1: a) Schematic for electrolyte gating of graphene and VO_2 based metasurfaces. The area of the devices is ∼1 cm × 0.5 cm. The gold side gate has approximately the same area as the sample (green). Contacts for voltage application were fabricated with silver paint at a distance of ∼5mm from each other. b) Phase diagram for VO_2 including dependence on vanadium oxidation state. Black line across the figure indicates the phase boundary between the insulating state and metallic state, around which the conductivity of metallic state is maximized. The dashed portion of the black line indicates inconsistent results between published sources. Our results in Figs. 2b and 3 are indicated by the red and pink solid arrows. The two red dashed arrows indicate our explanation for the results by Jeong et al [57].

4.3 Results and analysis

4.3.1 Summary

We first summarize our observations of gating effects on the graphene based metasurface response. Electrolyte gating of this graphene device is expected to cause solely electrostatic modification of the carrier concentration of graphene due to its excellent chemical stability [58]. The rising conductivity in graphene near the SRR gap is expected to progressively damp and ultimately short the LC resonant response of the device with increasing voltage. This resonance originates from the capacitive nature of the SRR gap and inductive nature of the SRR loop forming an effective LC circuit. The electrolyte gating response in one of the graphene metasurfaces is shown in Fig. 4.2a for several voltages given by $V = V_{\text{gate}} - V_{\text{CNP}}$, where V_{CNP} is the voltage of the charge neutrality point (CNP) (in our case $V_{\text{CNP}} \approx$ 1.2 V) at which the conductance of graphene is minimized. All spectra in Fig. 4.2a are normalized to the transmission at V_{CNP}. Due to the ambipolar nature of graphene, it is expected that the metasurface response should be symmetric for hole and electron doping. Our measurements are in accord with this expectation: the spectra for $V = -1.7$ V and $+1.7$ V are equidistant from the CNP, and display nearly identical frequency dependence. In contrast, the spectrum obtained at 0.7 V above V_{CNP} displays a response much closer to that of charge neutral graphene. We found that in gating of graphene, saturation of THz responses occurs within approximately 2 min of voltage application and the gating effect is fully reversible after the gate voltage is turned off. The 2 min saturation time of electrostatic doping in the graphene metasurface is a consequence of a relatively low diffusion coefficient of cation and anion motion in the ionic gel and the large functional area of the gating devices. Switching was possible on graphene devices as large as 1 cm^2. Since we probe our samples optically, we minimize the resistive heating of our devices, which can be a problem in transport measurements where a source-drain voltage is applied.

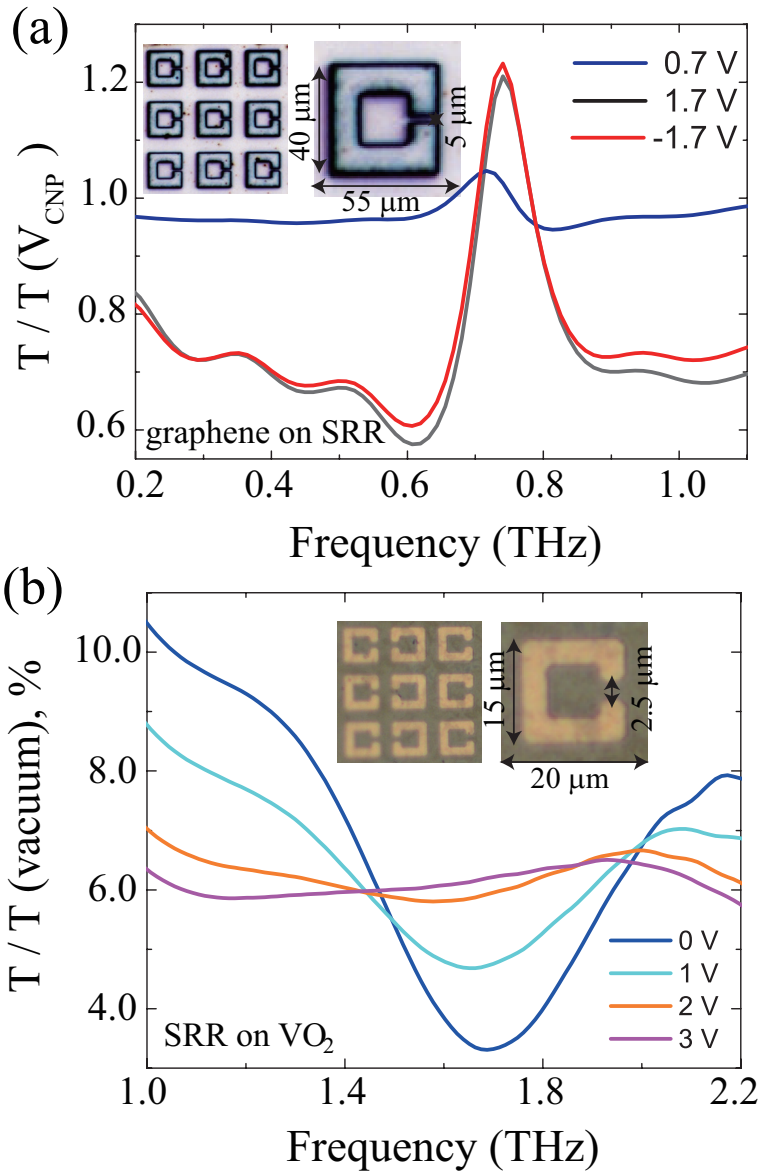

Figure 4.2: a) Voltage dependent THz transmission with a graphene-metasurface structure. Spectra are taken ∼2 min after voltage application when gating effects saturate ($V = V_{\text{gate}} - V_{\text{CNP}}$) and are normalized to THz transmission through graphene at the charge neutral point ($V_{\text{CNP}} = -1.2$ V). b) Voltage dependent THz transmission at 315K ($V = V_{\text{gate}}$). Spectra are taken ∼20 min after voltage application and normalized to THz transmission through air. The insets in (a) and (b) show photos of the gold SRR sitting beneath (on) graphene (VO_2) before the ionic gel is applied. The dimensions of the single SRR unit cell are also shown.

4.3.2 Effects of positive voltage

Next, we examine the voltage-dependent response of our VO_2 based device. VO_2 is a canonical insulator-metal phase transition (IMT) material [16, 59–64]. When the temperature is increased above 340K (T_{IMT}), the VO_2 conductivity increases by several orders of magnitude with a simultaneous increase in the permittivity. As mentioned above, we elect to use voltage across the interface between the film and electrolyte, as opposed to temperature, to induce the VO_2 IMT in our 90 nm sol-gel VO_2 film. We characterize our device response to voltage application at two different temperatures. We first fixed the device temperature at 315 K, below the IMT hysteresis as shown in the inset of Fig. 4.3a. Second, we keep the device within the hysteretic region of the IMT at a temperature of 336 K (inset of Fig. 4.3b). We start by summarizing the results of our voltage-induced experiments before giving a full analysis of the device at each of these temperatures. Positive voltage applied to the gold gate in pristine samples below T_{IMT} increases VO_2 metallicity, thereby switching off the SRR resonance. Negative voltages applied in the hysteretic region of the transition exhibit a delay on the order of 2 min in which the VO_2 conductivity slightly increases, followed by a dramatic reduction of the VO_2 conductivity (Fig. 4.1b). Additionally, the effects of positive voltage application can be reversed using a negative bias, but do not reverse with only bias removal. Finally, the effects of negative voltages applied at elevated temperatures near the phase transition are self-reversing after the voltage is removed.

We now analyze the THz transmission and the effects of electrolyte modification on the VO_2 metasurface at 315 K. The transmission spectra shown in Fig. 4.2b illustrate the changes to the metasurface response with positive voltages. Initially, at 0 V, the device displays a strong LC SRR resonance (similar to that seen in the graphene device), indicating that the VO_2 is in its insulating state and is well below the hysteretic region of the IMT. The overall slope seen in these spectra is a result of absorption by the ion gel, which decreases with increasing frequency. Changes in the resonant response of VO_2 hybrid devices arise directly from modification of the permittivity and conductivity of VO_2, which cause a redshift and damping of the SRR resonance, respectively [8, 15, 65]. Application of posi-

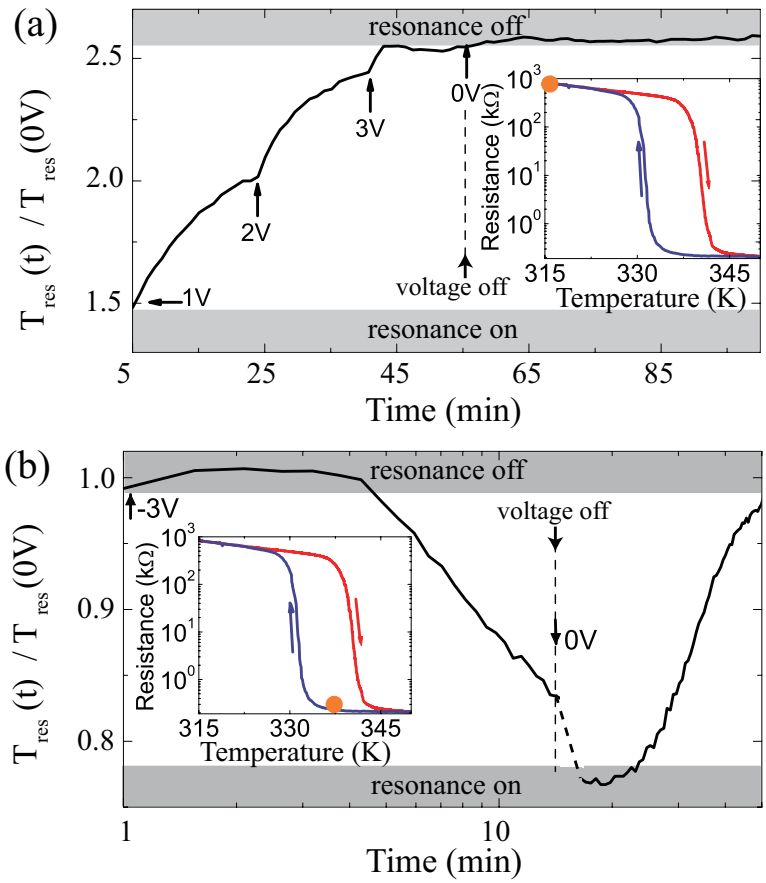

Figure 4.3: a) Time dependent on resonance transmission change $T_{res}(t)$ with various positive voltages at 315 K. Transmission is normalized to 0 V data $T_{res}(0\ V)$ before time zero. At each fixed voltage (1 V, 2 V, and 3 V), the rate of transmission change is different. The gating effect is non-reversible after the voltage is turned off. b) Time dependent normalized THz transmission of VO_2 metasurface structure at 336 K with the applied voltage fixed at -3 V. Initially, the transmission increases but then dramatically decreases. Reversibility is seen after the voltage is turned off. The insets in (a) and (b) show the corresponding temperatures at which data were taken indicated by the orange dots on the VO_2 temperature driven hysteresis curve.

tive voltages monotonically damps the SRR resonance with 3 V yielding complete suppression of this resonance. As we will discuss in detail later, this systematic suppression of the SRR resonance is attributed to reduction of the vanadium ions as the applied voltage drives VO_2 across the IMT following the pink solid line in Fig. 4.1b, which shows the oxidation state dependent conductance of VO_2.

4.3.3 Time dependence at low temperatures

To explore the underlying mechanism and compare to the voltage induced changes in the graphene-based devices, we performed time dependent measurement in our VO_2 based devices. Fig. 4.3a shows the time dependent normalized transmission at the resonance frequency at 315 K for various voltages. These data correspond to the spectra in Fig. 4.2b. The transmission at the resonance frequency continually increases with fixed positive bias, and the rate of this increase is greater for larger biases. After application of the maximum voltage of 3 V, the sample remained in the metallic state and the metasurface resonance remained damped even after 24 h at zero bias, provided the device was kept in vacuum. To reverse this change in VO_2 properties, application of a negative voltage was necessary to restore the resonance. Similar time dependent gating effects were observed when resetting the transmission of the devices with negative bias (not shown). This on/off switching of the SRR with oxidation/reduction of vanadium enables memory tuning of the device as reverse bias application is required to go back to the original state. Through modification of the duration and polarity of the applied voltage, one can precisely control the on-resonance transmission as well as the frequency of the metasurface resonance. This is in agreement with previous findings that positive voltages create oxygen vacancies and increase metallicity of VO_2 samples with non-self-healingreversibility [57]. It is worth noting that it took approximately 20 min to stabilize the device response after voltage application. This is in stark contrast to the $\sim$2 min saturation time for the electrostatic changes that dominates the response time in our graphene devices. Application of voltage for longer than 20 min results a plateau in the time dependent transmission at the resonance frequency.

4.3.4 Effects of negative voltages at elevated temperatures

We now discuss modification of the metasurface resonance at temperatures within the zero-bias hysteretic region of the VO_2 IMT (336 K). The device was first heated to well above the hysteretic region of the zero-bias transition (360 K), and then slowly cooled to 336 K, indicated by the orange circle in the inset of Fig. 4.3b where VO_2 remains predominantly metallic. Time dependent THz transmission spectra were collected at this temperature. Fig. 4.3b shows the time dependence of the on-resonance transmission (T_{res}) at a fixed applied voltage of 3 V, normalized to 0 V on resonance transmission. At this voltage, the resonance is first slightly damped, indicating an increase in the conductivity of VO_2. However, on longer time scales (>3 min), the resonance became significantly more pronounced indicating that the VO_2 is becoming more insulating. These changes in VO_2 properties are reflected in the slight upturn and sharp decrease in on resonance THz transmission in Fig. 4.3b. Removal of the applied voltage demonstrates the reversibility of the effects of negative voltage application at this temperature as shown in Fig. 4.3b. This is surprising, given the conclusion on non-reversibility of previous experiments [34, 57, 66], and the exact reason of this reversible hole doping in VO_2 still needs to be explored.

4.4 Conclusions

The dramatic difference between the saturation times in our VO_2 and graphene devices, as well as the ease of reversibility seen in graphene, indicate that alternative mechanisms outside of electrostatic modification must be at play. The voltage-induced behavior of the VO_2 metasurface at 336 K and 315 K can be understood in the picture of oxidation and reduction of vanadium ion V^{4+} through injection and removal of oxygen, as proposed in the diagram in Fig. 4.1b. For negative voltages, oxygen is added to the VO_2 film while for positive voltages, the oxygen in the film is depleted (e.g. For positive gate voltage, $VO_2 + 2xe \rightarrow VO_2 + xO^{2-}$). The oxidation (reduction) process undergone by our device with negative (positive) voltage application is shown by the solid blue (pink) arrow in Fig. 4.1b.

The diagonal black line (solid and dashed) stretching across this figure indicates the phase boundary corresponding to the maximum conductivity for a given vanadium oxidation state. From this, we can see that the initial upturn in on-resonance transmission at 336 K (Fig. 4.3b) results from reaching the maximum conductivity across the phase boundary before crossing into the insulating state, as indicated by the blue arrow. For comparison, previous results obtained on bare VO_2 on TiO_2 substrate at high and low temperatures by Jeong et al. [57] have also been indicated by the red dashed arrows in Fig. 4.1b.

In summary, we have demonstrated tunable metasurfaces via ionic gel based electrostatic and electrochemical effects. Both thermal and electrical tunability can be realized in our hybrid devices. This enables unprecedented control over the optical properties of these metasurfaces over a wide temperature range and sets the stage for the future use of electrolyte gating in THz photonic devices. Through integration of additional switching mechanisms and material properties such as light induced phase transitions [67] and electronic anisotropy [68, 69] in transition metal oxides, additional functionalities can be realized with more sophisticated electrolyte gating structures.

4.5 Acknowledgements

Chapter 4, in full, is a reprint of material as it appears in M. D. Goldflam, M. K. Liu, B. C. Chapler, H. T. Stinson, A. J. Sternbach, A. S. McLeod, J. D. Zhang, K. Geng, M. Royal, B.-J. Kim, R. D. Averitt, N. M. Jokerst, D. R. Smith, H.-T. Kim, and D. N. Basov. "Voltage switching of a VO_2 memory metasurface using ionic gel," *Applied Physics Letters*, 105(4):041117, July 2014. The dissertation author was the primary investigator and author of this publication.

Research at UCSD was supported by ARO, the Helmholtz Virtual Institute MEMRIOX, and the creative research project of ETRI.

Chapter 5

Tuning and Persistent Switching of Graphene Plasmons on a Ferroelectric Substrate

5.1 Introduction

Graphene plasmonics is a burgeoning field of study that has attracted significant interest due to graphene's unique electronic and optical properties, as well as the ability to conveniently modify these properties through back-gating or optical pumping [70–74]. Extensive work has been performed to characterize the capabilities of different gate dielectrics for tuning of the electronic properties of graphene. Among the most studied gate dielectrics are SiO_2, for its robustness with voltage application, and hexagonal boron nitride (hBN), for the high mobility it lends to graphene microcrystals or films [75–77]. However, the realization of practical plasmonic devices requires implementation of alternative dielectrics to achieve larger variance in graphene properties and to potentially attain additional control mechanisms (e.g., persistent effects). Ferroelectrics are one intriguing option. In general, such dielectrics have a large DC permittivity (κ or ϵ_{DC}) in the linear, low-field regime and also may enable persistent tuning in the high-field nonlinear regime [78–83]. As a result, ferroelectrics may find applications in graphene-based

electronics and plasmonics. Although previous experimental works on ferroelectric modification of graphene primarily investigated control of electronic properties [78–88], we focus here on the plasmonic and photonic response. We examined the potential for tuning of the plasmonic response of graphene through the use of one such dielectric, $PbZr_{0.3}Ti_{0.7}O_3$ (PZT). The dielectric constant of PZT can reach values of several hundred or thousand, many times that of SiO_2, making it an extremely effective insulator for back-gated structures [79]. Therefore, PZT's potency for use in future plasmonic devices warrants investigation.

5.2 Experimental details

5.2.1 Near-field microscopy

To characterize graphene plasmon propagation on PZT substrates, we employed scattering-type scanning near field optical microscopy (s-SNOM) [89–91]. In these measurements, infrared light is focused at the sharp apex of a metallic atomic force microscope (AFM) tip as seen in a 1a (Neaspec) [92–94]. A fraction of the incident radiation polarizes the tip and is confined to length scales on the order of the tip diameter (∼20 nm) where the tip interacts with the sample. As a result, the light scattered from the tip-sample system contains information on the sample properties at deeply subdiffraction limited length scales [93]. Additionally, through the enhanced range of momenta excited by the tip [74, 95, 96], it is possible to overcome the momentum mismatch between plasmonic modes and the incident far-field light allowing the tip to launch radially propagating plasmons, which are reflected from topographic and electronic features in the graphene (e.g. edges, wrinkles, folds, grain boundaries) as shown schematically in Fig. 5.1a [92]. These reflected waves create oscillations in the local electric field directly beneath the tip corresponding to a detected variation in near-field signal. Analysis of the oscillating near field signal yields information including the plasmon wavelength (λ_p) given by twice its periodicity as seen in Fig. 5.2, and corresponding damping coefficient, γ_p. Both these parameters are directly related to the properties of graphene, including the scattering rate and carrier density [74, 96].

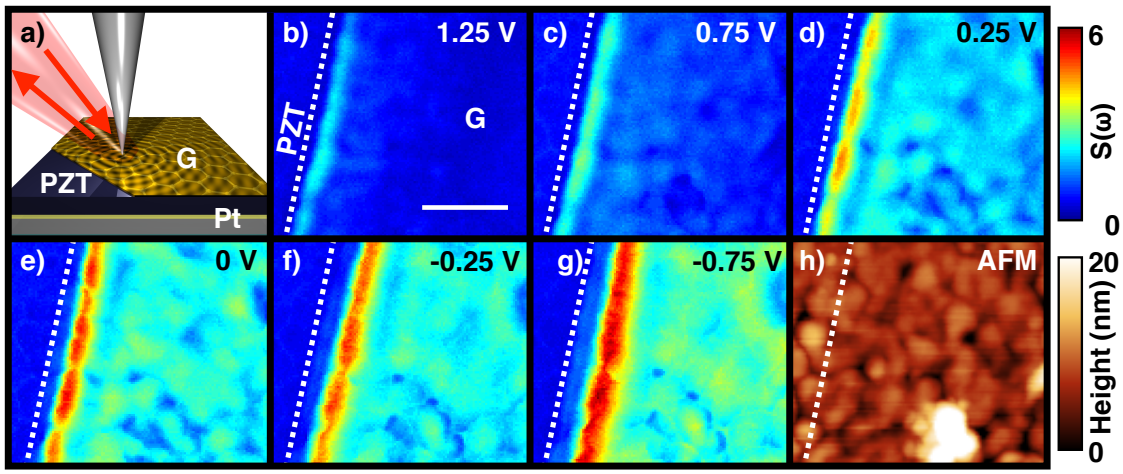

Figure 5.1: a) Schematic of our nano-imaging setup. The concentric yellow circles represent propagating plasmonic waves launched by the tip and reflected by the graphene edge. b-g) Normalized voltage dependent near-field amplitude (S(ω)) of graphene (right) on PZT (left) taken at $\omega = 890$ cm^{-1}. The dotted white line indicates the position of the graphene (denoted as G) edge determined from AFM. A strong plasmonic fringe is visible near this edge. Fringe brightness and width increase with decreasing voltage. h) AFM image, taken simultaneously with the 0 V data, showing device roughness in the same region as the SNOM images shown in b-g.

5.2.2 Sample details

Our device consists of a graphene microcrystals exfoliated on a 360 nm-thick polycrystalline PZT film grown via sol-gel on a 50 nm platinum layer that functions as our back-gate, as shown in the schematic in Fig. 5.1a. This back-gated structure allows for straightforward carrier doping of graphene in the linear dielectric regime of PZT (-1 V $< V_G <$ +1 V) during near-field measurements. To accurately probe graphene plasmons without the influence of plasmon–phonon coupling, which modifies the frequency–momentum dispersion of the graphene plasmon from the simple square-root dependence [95], the sample was probed using a coherent infrared beam generated by a CO_2 laser at $\omega = 890$ cm^{-1}, where no PZT phonons are present. We first characterized our device at back-gate voltages ranging from $V_G = -0.75$ V to 1.25 V, where negative and positive voltages indicate an increase or decrease in the hole concentration in the graphene. The resulting normalized near field amplitudes are shown in Fig. 5.1b-g. In these images, the near field signal is related to the local z-component of the electric field (E_z) beneath the tip, with higher signal generally relating to a higher E_z in graphene. An AFM image of the same region is shown in Fig. 5.1h.

5.3 Results

5.3.1 Gate dependent plasmonic imaging

We first survey the gross features present in the near field images. The most prominent aspect of these images is the bright fringe seen at the edge (white dotted line across each image) of the graphene flake. According to previous studies [74,96], they are formed due to interference between tip-launched and edge reflected plasmons. As the hole concentration (n), and therefore the graphene conductivity (σ), increases at more negative V_G, the width and intensity of these fringes, along with the overall graphene signal, monotonically grow in congruence with previous measurements of structures utilizing SiO_2 gate insulator. This monotonic change in n with V_G reveals that the Fermi energy (E_F) never crosses the charge neutrality

point (CNP), which would correspond to a reduction and subsequent enhancement of n. Rather, this result suggests a positive carrier sign at all gate voltages in this range and indicates unintentional hole doping of the graphene at 0 V. From near-field measurements over a broader voltage range, we expect that the voltage at the CNP is between 1.0 V and 1.5 V (see Appendix A). This is consistent with a minimal carrier concentration at $V_G = 1.25$ V, resulting in the near invisibility of graphene in Fig. 5.1b where only a weak fringe is visible, as charge neutral graphene is nearly infrared transparent, transmitting approximately 98% of incident light. The existence of a weak fringe in spite of low carrier concentration is likely due to edge doping, as was previously seen in graphene on SiO_2 [97,98] and is also reflected in the decreasing overall signal in regions of graphene away from the edge.

5.4 Analysis and discussion

5.4.1 Plasmon wavelength

To directly characterize plasmon behavior, we examined the near field signal close to the graphene edge where interference fringes are most prominent. The plasmon wavelength, λ_p, can be directly extracted from the images in Fig. 5.1b-g by obtaining a line profile of our SNOM signal perpendicular to the edge. Many such profiles are obtained and averaged to eliminate artifacts from variation in substrate topography and substrate optical properties. The resulting profile obtained from our 0 V data is plotted as the solid black curve in Fig. 5.2. This profile shows characteristic fringes, which decrease in amplitude with increasing distance from the graphene edge. Modification of the applied voltage results in variation of the amplitude and wavelength of the interference fringes. The values of λ_p extracted from the averaged line profiles extracted at each applied voltage are shown in the inset of Fig. 5.2. The measured wavelength varies by as much as $\pm 75\%$ of its value at 0 V with a voltage range of only ± 1 V. This is more than two orders of magnitude greater than what is seen in SiO_2 supported graphene structures for the same range of applied electric fields.

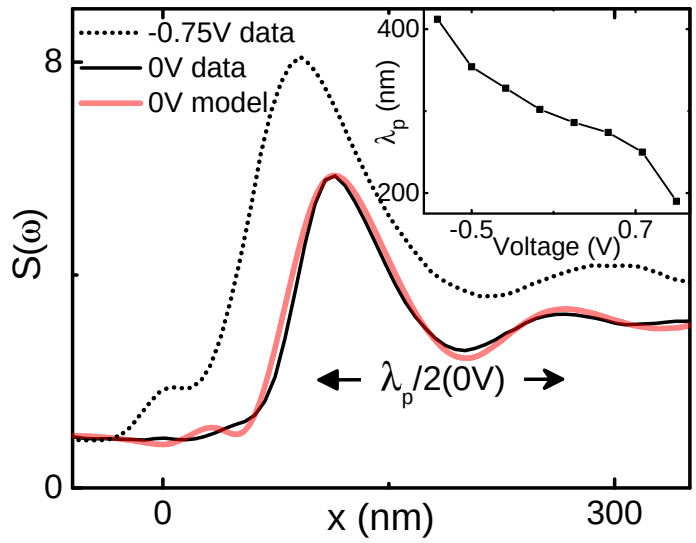

Figure 5.2: Comparison of simulated plasmonic profile (red) and data (solid black) taken from Fig. 5.1d with 0 V applied to the back gate. There is good agreement between the two profiles for $\gamma_p = 0.135$. The profile for the longest wavelength data (dotted black) is also shown. (Inset) Gate-dependent plasmonic wavelength obtained from the images in Fig. 5.1.

5.4.2 Extraction of PZT dielectric constant

The measurements reported in Figs. 5.1 and 5.2 can serve as an alternative method for directly determining the DC dielectric constant of PZT. The theoretical plasmon dispersion can be calculated from the maximum of the reflection coefficient, $R_p(\omega = 890\ \mathrm{cm}^{-1})$, which has a well-defined dependence on the graphene carrier concentration [70,74,95,99,100]. A comparison of this theoretical dispersion and the measured plasmon wavelength allows for extraction of the graphene carrier concentration, n, at each applied voltage, V_G. This carrier density then yields the dielectric constant of PZT: $\epsilon_{\mathrm{DC}} = (ned/|V_G - V_{\mathrm{CNP}}|)$ where e is the electron charge, d is the PZT thickness, and $V_{\mathrm{CNP}} = 1.3$ V consistent with our near field measurements. This analysis yields a range of values $\epsilon_{\mathrm{DC}} = 450 - 550$, well within the expected range for PZT and in agreement with direct measurements on similar films.

5.4.3 Details of plasmonic damping

In spite of the large wavelengths we observe in Figs. 5.1 and 5.2, the plasmon propagation length appears limited to ∼500 nm even for the longest $\lambda_p = 420$ nm (black dotted line in Fig. 5.2), indicating the presence of plasmonic scattering in these devices. Information on losses and scattering can be obtained by examining the decay in the interference fringe strength with increasing tip-to-edge distance. Although averaging many curves with slight variation in phase has the potential to mask intrinsic damping, a comparison of damping extracted from averaged and non-averaged data shows little variation in the plasmonic damping. To obtain the plasmon damping coefficient, γ_p, we modeled our plasmonic profile obtained at $V_G = 0$ V using the procedure outlined in Fei et al. [74], approximating the tip as an elongated ellipsoid [101]. The value of γ_p is varied until the theoretical fringe profile matches experimental data. The resulting simulated profile is shown by the red curve in Fig. 5.2 and fits our experimental data (solid black) most closely for $\gamma_p = 0.135$. The measured damping and wavelength are directly related to the plasmon dispersion via $\lambda_p = 2\pi/q_1$ and $\gamma_p = q_2/q_1$ and complex graphene conductivity, $\sigma = \sigma_1 + i\sigma_2$, with the theoretical dispersion given by

$$q_p = q_1 + q_1 = \frac{i\omega\left[1 + \epsilon(\omega)\right]}{4\pi\sigma(\omega)} \tag{5.1}$$

where $\omega = 890$ cm^{-1} is the excitation frequency and $\epsilon(890\text{ cm}^{-1}) = 2.58 + 0.12i$ is the ellipsometrically measured permittivity of the PZT at our probing frequency. At $V_G = 0$ V, the measured plasmon wavelength ($\lambda_p = 270$ nm) and damping ($\gamma_p = 0.135$) yield a graphene conductivity of $\sigma(890\text{ cm}^{-1}) = (0.56 + 5.8i) \times e^2/h$. The uncertainty in the extracted plasmon wavelength is ±30 nm and is a result of several factors including the tip radius (20 nm), which determines the resolution of our measurements. The conductivity, determined from near field data, can be compared to a semiclassical Drude model for graphene using a carrier relaxation rate, $\tau^{-1} = 70$ cm^{-1}, determined independently from the DC mobility of $\mu = 2000$ cm^2/(V·s) measured using transport in single grains of chemical vapor deposition grown graphene [79]. The conductivity from this model is given by

$$\sigma(\omega) = \frac{e^2 E_F}{\pi\hbar} \frac{i}{\omega + i\tau^{-1}} = (0.5 + 6.7i) \times e^2/h \tag{5.2}$$

where $E_F(0\ \mathrm{V}) = 3000\ \mathrm{cm}^{-1}$ is the graphene Fermi energy. Plasmonic damping originates from a combination of losses within graphene itself and those resulting from the dielectric environment around graphene as given by $\gamma_p \approx \sigma_1/\sigma_2 + (\epsilon_2/(1+\epsilon_1))$ with $\sigma_1/\sigma_2 = 0.098$ and $(\epsilon_2/(1+\epsilon_1)) = 0.037$ giving the relative contributions from each channel. Additionally, the agreement between the non-interacting Drude model and our measured conductivity indicates that damping in the graphene can be ascribed to the high scattering rate of the electron gas in graphene on PZT. In this regime of enhanced scattering, the many body interactions that were previously reported for graphene on SiO_2 [74] and hBN [102] do not play a significant role. Additionally, the absence of many body effects in our device can be understood as a direct result of the high dielectric constant of PZT, which serves to screen electron–electron interaction reducing the overall strength of the Coulomb force by several orders of magnitude as compared to structures using SiO_2 as the gate insulator [103].

5.4.4 Effects of PZT topography on plasmon propagation

Surprisingly, the value of the loss factor γ_p observed in our device is comparable to that measured by Fei et al [74]. However, in contrast to their results, it is difficult to distinguish fringes beyond the first directly in our imaging data. Examination of the internal regions of graphene shows the existence of bright fringes that are reminiscent of the plasmonic interference patterns observed at the edges of graphene flakes. These findings suggest the existence of plasmonic reflectors and scatterers within the interior of graphene, as these are a prerequisite for the formation of these additional interference patterns [104]. Initial examination of the data suggests a correlation between the underlying PZT grain topography and reflected plasmons. The AFM image in Fig. 5.1h shows a similar topographic landscape on bare PZT and graphene covered PZT, indicating that graphene sits closely to the surface of PZT, directly following the grain structure below it. The surface roughness of PZT is ∼4 nm across the 1×1 μm region shown in Fig.

5.1h with similar roughness reflected in the graphene. Individual PZT grains are visible in topography within both regions, with dimensions on the order of tens of nanometers.

To verify PZT grain boundaries as the source of plasmonic reflection within the interior of graphene, conventional Laplacian edge detection techniques were applied to the AFM data in Fig. 5.1h resulting in the processed image in Fig. 5.3a [105, 106]. The white traces running throughout this panel indicate the edges of PZT grains. In order to determine the relationship between the bright fringes in the graphene interior and the PZT grains, we overlaid the near field image from Fig. 5.1g on top of the processed AFM image to create Fig. 5.3b. In this image, the PZT grain edges are simultaneously visible with the near field signal. The bright features in the interior of graphene appear to be enclosed within PZT grains suggesting that plasmons are reflected at the boundaries of these grains. This points to two possible sources of plasmonic reflection within the interior of graphene, both of which are governed by the existence of PZT grains: (1) topographic variation created in graphene by PZT creates strong enough variation in local graphene conductivity (from strain or other effects) to reflect plasmons and (2) different grains in PZT are polarized differently causing local conductivity changes which reflect plasmons. These two sources are difficult to distinguish with our current measurements, requiring alternative techniques, but do not modify the analysis described here.

For such analysis to hold, trivial topographical influence on near field signal [107] must be accounted for as topographic variation can modify the collected near field signal. In general, concave surface features create higher near field signal resulting from field enhancement, whereas convex surfaces result in lower signal. This is in contrast to what we observe with higher signal concentrated in the central convex regions of the PZT grains. Our analysis, therefore, suggests that PZT created graphene conductivity variation is a significant source of plasmonic reflection within the interior of graphene. Scattering from these local conductivity changes exacerbates the task of distinguishing multiple fringes close to the edge in the near field images without averaged profiles as the additional reflectors can

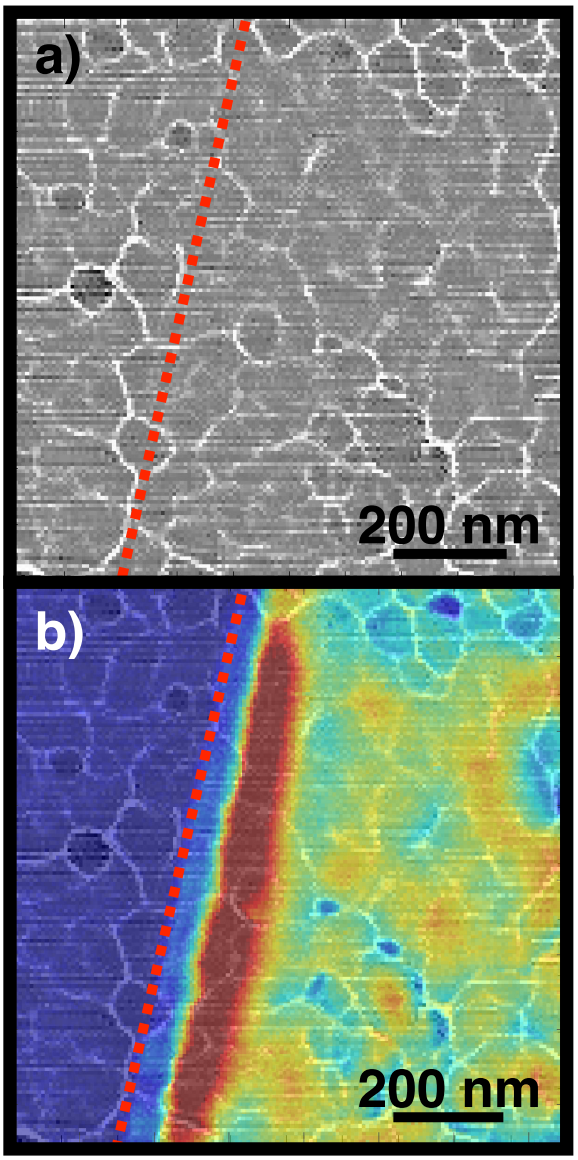

Figure 5.3: a) Image obtained from conventional Laplacian edge detection techniques performed on topography from Fig. 5.1h. Grain borders shown by white lines throughout image. b) Near field signal from Fig. 5.1g overlaid on the processed topography shown in (a).

deflect propagating plasmons before they are able to make the round trip from the tip to the edge and back. The observation of rapid plasmon decoherence in our near field images, compared with that in SiO_2 and resulting from scattering from PZT grains, suggests that significant improvement in the observed propagation length may be achieved by using graphene on atomically flat epitaxial PZT giving plasmons a smooth surface across which they can propagate [81].

5.4.5 Persistent plasmon tuning through ferroelectric polarization switching

In spite of the significant scattering resulting from topographic features, we were able to employ ferroelectric switching of PZT for persistent tuning of graphene plasmons. As a ferroelectric material, PZT can be persistently polarized with application of transient electric fields greater than ∼30 kV/cm (1 V across our device). It was previously demonstrated that this field application modifies the voltage of the graphene CNP, producing a corresponding change in the graphene carrier concentration and plasmonic characteristics, even after removal of the voltage [78, 79, 82, 108].

To test the possibility of plasmonic memory gating, we first obtained a near field image of an unpolarized region of the device at 0 V. After this measurement, a gate voltage of 2 V was applied for several minutes to polarize the PZT. Although the fairly low field from application of 2 V to our PZT film is not sufficient for complete polarization, it is larger than the coercive field of PZT and should therefore be enough to partially and persistently align the dipoles within the film (see Appendix A). Following voltage removal, a second image was obtained in the same region of the device. Because the application of positive voltages reduces the hole concentration, any film polarization remaining after voltage application should result in a similar decrease in near field signal as that seen with increasingly positive V_G in our continuous bias application measurements in Fig. 5.1b-g. The two near field images taken before and after memory gating, and their corresponding profiles, are shown in Fig. 5.4a–d. Prior to voltage application, a bright fringe is visible in Fig. 5.4a with multiple maxima seen in the corresponding line

profile shown in Fig. 5.4c. The equivalent data taken after voltage removal, Fig. 5.4b and d, respectively, demonstrate significant reduction in fringe strength and overall graphene brightness, as well as the disappearance of the second fringe in the line profile. These changes are consistent with a reduction in the magnitude of graphene doping, a quantity to which our near-field data is extremely sensitive. Thus, these data demonstrate the ability to persistently turn off the plasmonic response with transient voltage application. These changes to graphene carrier concentration were reversible with negative bias application and faded with extended 0 V bias application as seen in other ferroelectric based devices [109]. This time dependent relaxation is consistent with the following picture of partial PZT polarization. Initial application of 2 V begins to reorient the polarization of each PZT grain into the out of plane direction. With removal of the driving voltage, the polarization directions of the grains relax back to their original disordered lower energy state. This mechanism can be further verified through the implementation of simultaneous piezoresponse force microscopy and plasmonic near-field studies. With position dependent control of PZT polarization, as has been demonstrated using AFM [110, 111], such plasmonic memory gating could be employed for the creation of reconfigurable plasmonic nanocircuits without the need for continuous stimulus.

5.5 Conclusions

These results demonstrate the effectiveness of PZT as a gate dielectric for control of graphene plasmons. The dramatic increase in tunability, arising from the large dielectric constant of PZT, minimizes the voltages necessary for significant modification of plasmonic response. Additionally, the potential for persistent modification of plasmonic properties with polarization of ferroelectric films presents the opportunity for creation of a variety of graphene based nanoplasmonic elements (circuits, reflectors, and lenses). Although losses are present in our device, exfoliation of graphene on atomically flat epitaxial PZT [112–114] could dramatically reduce unwanted plasmonic scattering, making PZT an ideal substrate for low

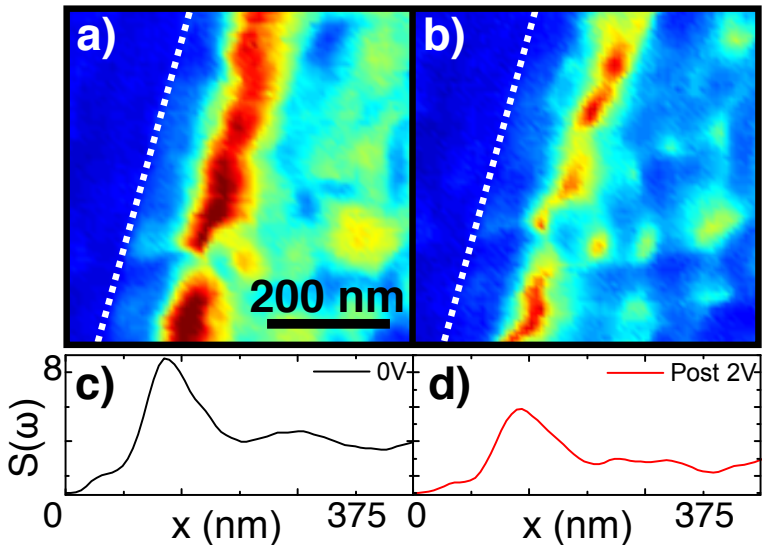

Figure 5.4: a) Normalized near field amplitude of graphene on an unpolarized region of PZT. b) Second image taken in the same region as (a) after application and removal of 2 V across PZT. c) and d) Line profiles corresponding to the plasmonic fringe seen in (a) and (b), respectively.

voltage graphene based electronic applications.

5.6 Acknowledgements

Chapter 5, in full, is a reprint of material as it appears in M. D. Goldflam, G.-X. Ni, K. W. Post, Z. Fei, Y. Yeo, J. Y. Tan, A. S. Rodin, B. C. Chapler, B. Özyilmaz, A. H. Castro Neto, M. M. Fogler, and D. N. Basov, "Tuning and Persistent Switching of Graphene Plasmons on a Ferroelectric Substrate," *Nano Letters*, vol. 15, no. 8, pp. 48594864, 2015. The dissertation author was the primary investigator and author of this publication.

Work supported by ONR (N00014-13-1-0464). Instrument development at UCSD is supported by DOE-BES. B.Ö. acknowledges support by the NUS Young Investigator Award and the SMF-NUS Research Horizons Award 2009-Phase II. A.H.C.N. acknowledges the National Research Foundation, Prime Ministers Office, Singapore, under its Medium Sized Centre Programme and CRP award "Novel 2D materials with tailored properties: beyond graphene" (R-144-000-295-281).

Appendix A

Supplementary information for Chapter 5

A.1 Electrical transport measurement results

Electrical transport curves collected on four-terminal graphene field-effect transistor (GFET) devices on identical PZT substrates as those measured in near-field microscopy are shown in Fig S1. These R vs V_G curves demonstrate the response of the GFET/PZT device in both the linear dielectric regime (Fig. A.1a: -1 V $< V_G <$ 1 V), as well as in the range where PZT begins to polarize (Fig A.1b: -2 V $< V_G <$ 2 V). The data within the linear regime show one clearly defined maximum in resistance indicating a lack of polarization of the PZT film. In contrast, the larger sweep range reveals the existence of two maxima indicating partial polarization of the dielectric layer [79,108]. The observed anti-hysteresis in this transport data, as compared to the ferroelectric hysteresis we observed in our near-field data, is likely a result of different fabrication methods, taken to ensure compatibility with our near-field microscope and enable optimal plasmonic characterization. Specifically, the CVD graphene used for transport was wet transferred onto a PZT film. In contrast, for near-field measurements, graphene was exfoliated and dry transferred onto heated PZT to obtain optimally clean graphene, a necessity for clear plasmon propagation.

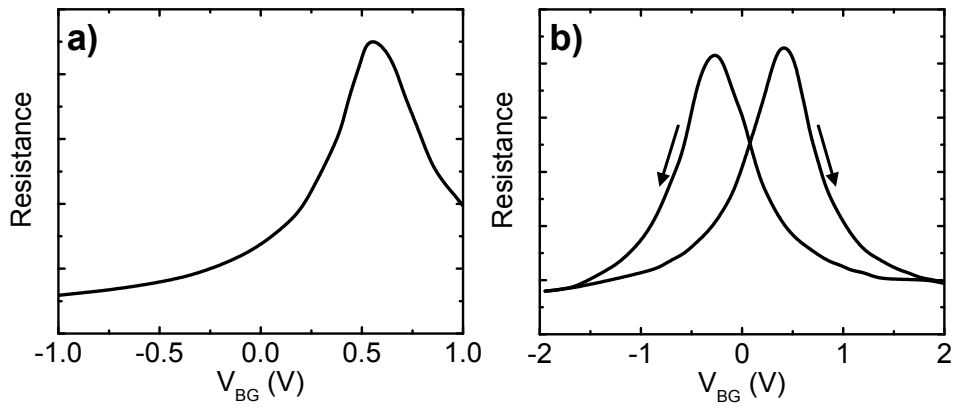

Figure A.1: Dependence of graphene resistance on voltage sweep range in wet transferred CVD sample. a) Voltage sweep within the linear regime between -1 V and 1 V. b) Resistance measured during a voltage sweep from -2 V to 2 V.

A.2 Average near-field signal dependence on gate voltage

The hysteresis present in our near-field device can be observed by examining the voltage dependent normalized near-field signal of graphene, $S(\omega)$, which is given by the ratio of the graphene signal to that of PZT and is collected at a probing frequency of 890 cm^{-1}. In order to eliminate the effects of plasmonic reflection at the edge of graphene, these data are obtained in the interior regions of graphene, far from the edge. To account for topographic variation and changes in local properties of the samples, the values used in determining $S(\omega)$ are averages of the near-field signal obtained from images containing multiple PZT grains in each region of the device (graphene-covered and bare PZT). Identical areas were used at each voltage. As an analog to conventional transport data, we plot this data as $1/S(\omega)$, which varies similarly with doping to graphene conductivity and is shown in Fig. A.2. These data, acquired for 0 V $< V_G <$ 1 V, demonstrate the presence of a clear hysteresis between the two voltage sweep directions that is consistent with ferroelectric effects in our PZT film and also serve as a means of approximating the voltage of the charge neutrality point in our graphene sample. This V_{CNP} is obtained from the peak position in our $1/S(\omega)$ data and yields a value in the range of 1 V – 1.5 V.

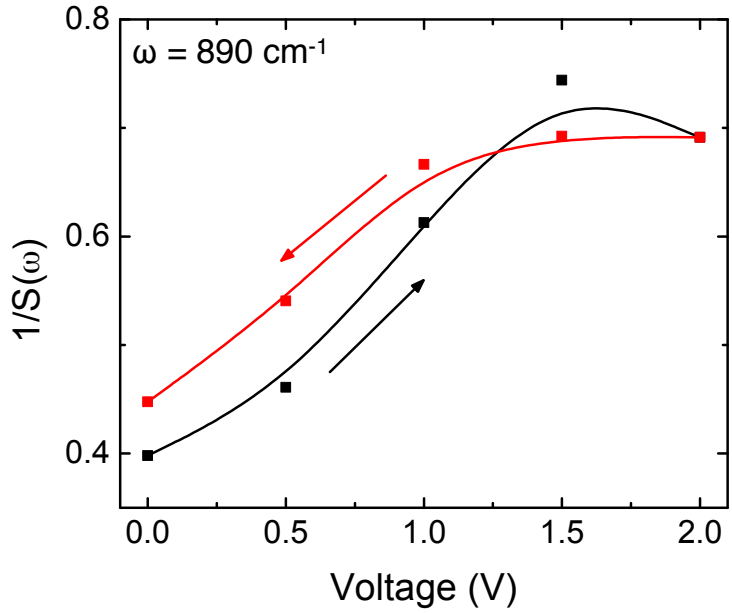

Figure A.2: Voltage dependence of the normalized near-field signal in the interior of the graphene flake for backgate voltages between 0 V and 2 V.

A.3 Optical properties of PZT

In order to understand the expected optical response of the graphene/PZT system, it is important to know the complex permittivity, $\epsilon(\omega) = \epsilon_1 + \epsilon_2$, of PZT prior to performing near field measurements. While the theoretical response of graphene is well understood, in practice, the response depends heavily on graphene's environment and therefore it is useful to understand this through methods outside of near field microscopy. A well established method of obtaining $\epsilon(\omega)$ is ellipsometry. The ellipsometrically measured permittivity of our PZT film is shown in Fig. A.3. This data shows the presence of several PZT phonons at frequencies below 850 cm^{-1} with significantly smaller variation in the permittivity above this frequency. By performing our near-field measurements above this frequency at $\omega = 890$ cm^{-1}, we avoid the effects of plasmon-phonon coupling. The theoretical plasmon dispersion, calculated as the maxima of the reflection coefficient, for our multilayer system is shown in Fig. A.4 [95].

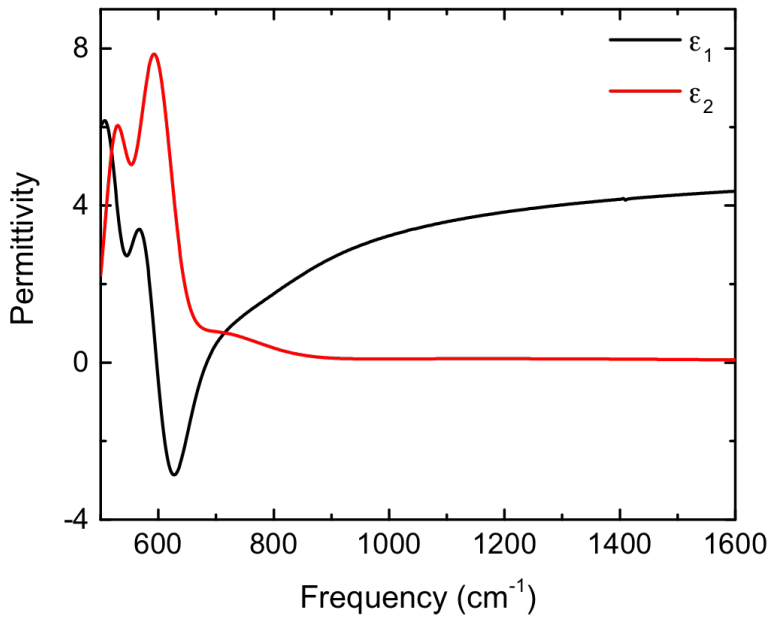

Figure A.3: Ellipsometrically measured complex permittivity of our PZT thin film.

A.4 Acknowledgements

Appendix A, in part, is a reprint of material as it appears in M. D. Goldflam, G.-X. Ni, K. W. Post, Z. Fei, Y. Yeo, J. Y. Tan, A. S. Rodin, B. C. Chapler, B. Özyilmaz, A. H. Castro Neto, M. M. Fogler, and D. N. Basov, "Tuning and Persistent Switching of Graphene Plasmons on a Ferroelectric Substrate," *Nano Letters*, vol. 15, no. 8, pp. 48594864, 2015. The dissertation author was the primary investigator and author of this publication.

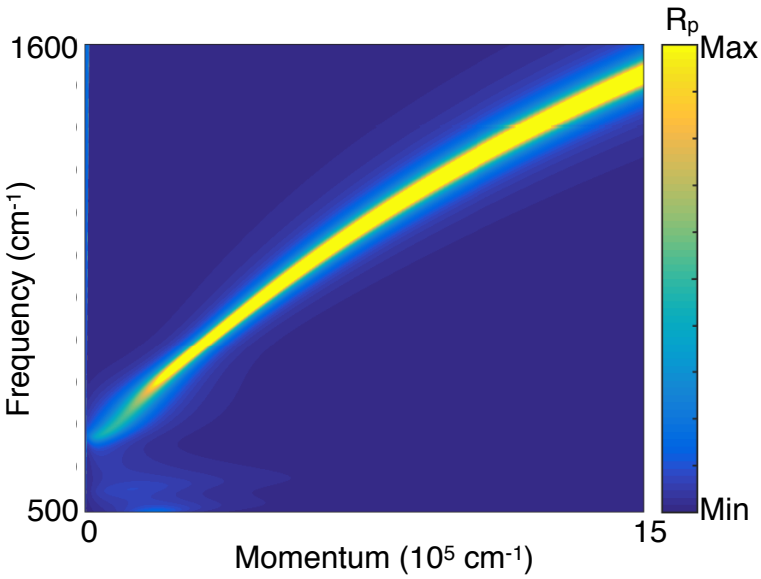

Figure A.4: Imaginary part of the reflection coefficient from our multilayer structure with a graphene Fermi energy of $E_F = 2000$ cm^{-1}. Maxima indicate the plasmon dispersion.

Bibliography

[1] V. Shalaev, "Optical negative-index metamaterials," *Nature photonics*, 2007.

[2] J. Pendry, "Negative refraction makes a perfect lens," *Physical review letters*, vol. 85, pp. 3966–9, Oct. 2000.

[3] M. C. K. Wiltshire, "Radio frequency (RF) metamaterials," *Physica Status Solidi (B) Basic Research*, vol. 244, no. 4, pp. 1227–1236, 2007.

[4] K. Sato, S. Yonak, and T. Nomura, "Metamaterials for automotive applications," *Antennas and Propagation Society International Symposium, 2007 IEEE*, pp. 1144–1147.

[5] D. Schurig, J. J. Mock, B. J. Justice, S. A. Cummer, J. B. Pendry, A. F. Starr, and D. R. Smith, "Metamaterial electromagnetic cloak at microwave frequencies.," *Science (New York, N.Y.)*, vol. 314, pp. 977–80, Nov. 2006.

[6] Z. Liu, H. Lee, Y. Xiong, C. Sun, and X. Zhang, "Far-field optical hyperlens magnifying sub-diffraction-limited objects," *Science*, vol. 315, no. 5819, p. 1686, 2007.

[7] I. V. Shadrivov, S. K. Morrison, and Y. S. Kivshar, "Tunable split-ring resonators for nonlinear negative-index metamaterials," *Optics Express*, vol. 14, no. 20, p. 9344, 2006.

[8] M. J. Dicken, K. Aydin, I. M. Pryce, L. A. Sweatlock, E. M. Boyd, S. Walavalkar, J. Ma, and H. A. Atwater, "Frequency tunable near-infrared metamaterials based on VO_2 phase transition.," *Optics express*, vol. 17, pp. 18330–9, Sept. 2009.

[9] T. Driscoll, D. N. Basov, A. F. Starr, P. M. Rye, S. Nemat-Nasser, D. Schurig, and D. R. Smith, "Free-space microwave focusing by a negative-index gradient lens," *Applied Physics Letters*, vol. 88, no. 8, p. 081101, 2006.

[10] T. J. Yen, W. J. Padilla, N. Fang, D. C. Vier, D. R. Smith, J. B. Pendry, D. N. Basov, and X. Zhang, "Terahertz magnetic response from artificial materials.," *Science (New York, N.Y.)*, vol. 303, pp. 1494–6, Mar. 2004.

[11] D. Smith, W. Padilla, D. Vier, S. Nemat-Nasser, and S. Schultz, "Composite medium with simultaneously negative permeability and permittivity," *Physical review letters*, vol. 84, pp. 4184–7, May 2000.

[12] D. Basov, R. Averitt, D. van der Marel, M. Dressel, and K. Haule, "Electrodynamics of correlated electron materials," *Reviews of Modern Physics*, vol. 83, pp. 471–542, June 2011.

[13] H.-T. Kim, B.-J. Kim, S. Choi, B.-G. Chae, Y. W. Lee, T. Driscoll, M. M. Qazilbash, and D. N. Basov, "Electrical oscillations induced by the metal-insulator transition in VO_2," *Journal of Applied Physics*, vol. 107, no. 2, p. 023702, 2010.

[14] M. Qazilbash, M. Brehm, G. Andreev, A. Frenzel, P.-C. Ho, B.-G. Chae, B.-J. Kim, S. Yun, H.-T. Kim, A. Balatsky, O. Shpyrko, M. Maple, F. Keilmann, and D. Basov, "Infrared spectroscopy and nano-imaging of the insulator-to-metal transition in vanadium dioxide," *Physical Review B*, vol. 79, p. 075107, Feb. 2009.

[15] T. Driscoll, H.-T. H. Kim, B. B.-G. Chae, B.-J. B. Kim, Y.-W. Lee, N. M. Jokerst, S. Palit, D. R. Smith, M. Di Ventra, and D. N. Basov, "Memory metamaterials," *Science (New York, N.Y.)*, vol. 325, no. 5947, p. 1518, 2009.

[16] H.-T. Kim, B.-G. Chae, D.-H. Youn, S.-L. Maeng, G. Kim, K.-Y. Kang, and Y.-S. Lim, "Mechanism and observation of Mott transition in VO_2-based two- and three-terminal devices," *New J. Phys.*, vol. 6, p. No pp. given, 2004.

[17] T. Driscoll, S. Palit, M. M. Qazilbash, M. Brehm, F. Keilmann, B.-G. Chae, S.-J. Yun, H.-T. Kim, S. Y. Cho, N. M. Jokerst, D. R. Smith, and D. N. Basov, "Dynamic tuning of an infrared hybrid-metamaterial resonance using vanadium dioxide," *Applied Physics Letters*, vol. 93, no. 2, p. 024101, 2008.

[18] R. Liu, T. Cui, D. Huang, B. Zhao, and D. Smith, "Description and explanation of electromagnetic behaviors in artificial metamaterials based on effective medium theory," *Physical Review E*, vol. 76, p. 026606, Aug. 2007.

[19] D. R. Smith, "Analytic expressions for the constitutive parameters of magnetoelectric metamaterials," *Physical Review E*, vol. 81, p. 036605, Mar. 2010.

[20] S. O'Brien and J. Pendry, "Magnetic activity at infrared frequencies in structured metallic photonic crystals," *Journal of Physics: Condensed Matter*, vol. 6383, 2002.

[21] W. J. Padilla, A. J. Taylor, and R. D. Averitt, "Dynamical Electric and Magnetic Metamaterial Response at Terahertz Frequencies," *Physical Review Letters*, vol. 96, pp. 1–4, Mar. 2006.

[22] H.-T. Chen, H. Yang, R. Singh, J. OHara, A. Azad, S. Trugman, Q. Jia, and A. Taylor, "Tuning the Resonance in High-Temperature Superconducting Terahertz Metamaterials," *Physical Review Letters*, vol. 105, pp. 1–4, Dec. 2010.

[23] R. A. Shelby, D. R. Smith, and S. Schultz, "Experimental verification of a negative index of refraction.," *Science (New York, N.Y.)*, vol. 292, pp. 77–9, Apr. 2001.

[24] V. Nguyen, B. Justice, S. Yonak, and D. Smith, "Electrically Coupled Graded Index Metamaterial," *2008 International Workshop on Antenna Technology: Small Antennas and Novel Metamaterials*, pp. 119–122, Mar. 2008.

[25] R. Liu, X. M. Yang, J. G. Gollub, J. J. Mock, T. J. Cui, and D. R. Smith, "Gradient index circuit by waveguided metamaterials," *Applied Physics Letters*, vol. 94, no. 7, p. 073506, 2009.

[26] J. Neu, B. Krolla, O. Paul, B. Reinhard, R. Beigang, and M. Rahm, "Metamaterial-based gradient index lens with strong focusing in the THz frequency range," *Optics Express*, vol. 18, no. 26, pp. 27748–27757, 2010.

[27] S. Sun, Q. He, S. Xiao, Q. Xu, X. Li, and L. Zhou, "Gradient-index metasurfaces as a bridge linking propagating waves and surface waves.," *Nature materials*, vol. 11, pp. 426–31, May 2012.

[28] H.-T. Chen, W. J. Padilla, J. M. O. Zide, A. C. Gossard, A. J. Taylor, and R. D. Averitt, "Active terahertz metamaterial devices," *Nature*, vol. 444, pp. 597–600, Nov. 2006.

[29] N. Wiwatcharagoses, K. Y. Park, and P. Chahal, "A new metamaterial unit cell for compact microstrip circuit designs," *Electronic Components and Technology Conference (ECTC), 2011 IEEE 61st*, pp. 169–172, May 2011.

[30] I. Gil and J. Bonache, "Tunable metamaterial transmission lines based on varactor-loaded split-ring resonators," *IEEE Transactions on Microwave Theory and Techniques*, vol. 54, no. 6, pp. 2665–2674, 2006.

[31] N. M. Litchinitser, I. R. Gabitov, A. I. Maimistov, and V. M. Shalaev, "Effect of an optical negative index thin film on optical bistability.," *Optics letters*, vol. 32, pp. 151–3, Jan. 2007.

[32] L. Carignan and A. Yelon, "Ferromagnetic nanowire metamaterials: theory and applications," *IEEE Transactions on Microwave Theory and Techniques*, vol. 59, no. 10, pp. 2568–2586, 2011.

[33] B.-J. Kim, Y. Lee, S. Choi, J.-W. Lim, S. Yun, H.-T. Kim, T.-J. Shin, and H.-S. Yun, "Micrometer x-ray diffraction study of VO_2 films: Separation between metal-insulator transition and structural phase transition," *Physical Review B*, vol. 77, pp. 1–5, June 2008.

[34] M. M. Qazilbash, Z. Q. Li, V. Podzorov, M. Brehm, F. Keilmann, B. G. Chae, H. T. Kim, and D. N. Basov, "Electrostatic modification of infrared response in gated structures based on VO_2," *Applied Physics Letters*, vol. 92, no. 24, p. 241906, 2008.

[35] M. D. Goldflam, T. Driscoll, B. Chapler, O. Khatib, N. Marie Jokerst, S. Palit, D. R. Smith, B.-J. Kim, G. Seo, H.-T. Kim, M. D. Ventra, and D. N. Basov, "Reconfigurable gradient index using VO_2 memory metamaterials," *Applied Physics Letters*, vol. 99, no. 4, p. 044103, 2011.

[36] A. Degiron, J. J. Mock, and D. R. Smith, "Modulating and tuning the response of metamaterials at the unit cell level," *Optics Express*, vol. 15, no. 3, p. 1115, 2007.

[37] N. Yu, P. Genevet, M. A. Kats, F. Aieta, J.-P. Tetienne, F. Capasso, and Z. Gaburro, "Light propagation with phase discontinuities: generalized laws of reflection and refraction.," *Science (New York, N.Y.)*, vol. 334, pp. 333–7, Oct. 2011.

[38] C. H. Ahn, J.-M. Triscone, and J. Mannhart, "Electric field effect in correlated oxide systems.," *Nature*, vol. 424, pp. 1015–8, Aug. 2003.

[39] Y. Zhou and S. Ramanathan, "Correlated Electron Materials and Field Effect Transistors for Logic: A Review," *Critical Reviews in Solid State and Materials Sciences*, vol. 38, pp. 286–317, Jan. 2013.

[40] O. Paul, C. Imhof, B. Lgel, S. Wolff, J. Heinrich, S. Hofling, A. Forchel, R. Zengerle, R. Beigang, and M. Rahm, "Polarization-independent active metamaterial for high-frequency terahertz modulation," *Optics express*, vol. 17, no. 2, pp. 819–827, 2009.

[41] T. Fujimoto and K. Awaga, "Electric-double-layer field-effect transistors with ionic liquids.," *Physical chemistry chemical physics : PCCP*, vol. 15, pp. 8983–9006, June 2013.

[42] K. H. Lee, M. S. Kang, S. Zhang, Y. Gu, T. P. Lodge, and C. D. Frisbie, ""Cut and stick" rubbery ion gels as high capacitance gate dielectrics.," *Advanced materials (Deerfield Beach, Fla.)*, vol. 24, pp. 4457–62, Aug. 2012.

[43] R. Scherwitzl, P. Zubko, I. G. Lezama, S. Ono, A. F. Morpurgo, G. Catalan, and J.-M. Triscone, "Electric-field control of the metal-insulator transition in ultrathin $NdNiO_3$ films.," *Advanced materials (Deerfield Beach, Fla.)*, vol. 22, pp. 5517–20, Dec. 2010.

[44] A. Dhoot, C. Israel, X. Moya, N. Mathur, and R. Friend, "Large Electric Field Effect in Electrolyte-Gated Manganites," *Physical Review Letters*, vol. 102, p. 136402, Mar. 2009.

[45] M. Lee, J. R. Williams, S. Zhang, C. D. Frisbie, and D. Goldhaber-Gordon, "Electrolyte Gate-Controlled Kondo Effect in $SrTiO_3$," *Physical Review Letters*, p. 256601, Dec.

[46] J. T. Ye, S. Inoue, K. Kobayashi, Y. Kasahara, H. T. Yuan, H. Shimotani, and Y. Iwasa, "Liquid-gated interface superconductivity on an atomically flat film," *Nature materials*, vol. 9, pp. 125–8, Feb. 2010.

[47] A. Beck, J. G. Bednorz, C. Gerber, C. Rossel, and D. Widmer, "Reproducible switching effect in thin oxide films for memory applications," *Applied Physics Letters*, vol. 77, no. 1, p. 139, 2000.

[48] J. J. Yang, D. B. Strukov, and D. R. Stewart, "Memristive devices for computing," *Nature nanotechnology*, vol. 8, pp. 13–24, Jan. 2012.

[49] W. C. Chien, Y. C. Chen, E. K. Lai, F. M. Lee, Y. Y. Lin, A. T. H. Chuang, K. P. Chang, Y. D. Yao, T. H. Chou, H. M. Lin, M. H. Lee, Y. H. Shih, K. Y. Hsieh, and C.-Y. Lu, "A study of the switching mechanism and electrode material offully CMOS compatible tungsten oxide ReRAM," *Applied Physics A*, vol. 102, pp. 901–907, Jan. 2011.

[50] M.-J. Lee, C. B. Lee, D. Lee, S. R. Lee, M. Chang, J. H. Hur, Y.-B. Kim, C.-J. Kim, D. H. Seo, S. Seo, U.-I. Chung, I.-K. Yoo, and K. Kim, "A fast, high-endurance and scalable non-volatile memory device made from asymmetric Ta_2O_{5-x}/TaO_{2-x} bilayer structures.," *Nature materials*, vol. 10, no. 8, pp. 625–630, 2011.

[51] J. J. Yang, F. Miao, M. Pickett, A. O. Douglas, D. R. Stewart, C. N. Lau, and R. S. Williams, "The mechanism of electroforming of metal oxide memristive switches," *Nanotechnology*, vol. 20, p. 215201, May 2009.

[52] D. M. Newns, J. A. Misewich, C. C. Tsuei, A. Gupta, B. A. Scott, and A. Schrott, "Mott transition field effect transistor," *Applied Physics Letters*, vol. 73, no. 6, p. 780, 1998.

[53] J. D. Yuen, A. S. Dhoot, E. B. Namdas, N. E. Coates, M. Heeney, I. McCulloch, D. Moses, and A. J. Heeger, "Electrochemical doping in electrolyte-gated polymer transistors.," *Journal of the American Chemical Society*, vol. 129, pp. 14367–71, Nov. 2007.

[54] M. L. T. Asaki, A. Redondo, T. A. Zawodzinski, and A. J. Taylor, "Dielectric relaxation and underlying dynamics of acetonitrile and 1-ethyl-3-methylimidazolium triflate mixtures using THz transmission spectroscopy," *The Journal of Chemical Physics*, vol. 116, no. 23, p. 10377, 2002.

[55] A. Stoppa, J. Hunger, R. Buchner, G. Hefter, A. Thoman, and H. Helm, "Interactions and dynamics in ionic liquids.," *The journal of physical chemistry. B*, vol. 112, pp. 4854–8, Apr. 2008.

[56] B. C. Chapler, S. Mack, L. Ju, T. W. Elson, B. W. Boudouris, E. Namdas, J. D. Yuen, A. J. Heeger, N. Samarth, M. Di Ventra, R. A. Segalman, D. D. Awschalom, F. Wang, and D. N. Basov, "Infrared conductivity of hole accumulation and depletion layers in (Ga,Mn)As- and (Ga,Be)As-based electric field-effect devices," *Physical Review B*, vol. 86, p. 165302, Oct. 2012.

[57] J. Jeong, N. Aetukuri, T. Graf, T. D. Schladt, M. G. Samant, and S. S. P. Parkin, "Suppression of metal-insulator transition in VO_2 by electric field-induced oxygen vacancy formation.," *Science (New York, N.Y.)*, vol. 339, pp. 1402–5, Mar. 2013.

[58] N. K. Emani, T.-F. Chung, A. V. Kildishev, V. M. Shalaev, Y. P. Chen, and A. Boltasseva, "Electrical modulation of fano resonance in plasmonic nanostructures using graphene.," *Nano letters*, vol. 14, pp. 78–82, Jan. 2014.

[59] M. Qazilbash, M. Brehm, B.-G. Chae, P.-C. Ho, G. Andreev, B.-J. Kim, S. J. Yun, A. Balatsky, M. Maple, F. Keilmann, H.-T. Kim, and D. N. Basov, "Mott transition in VO_2 revealed by infrared spectroscopy and nano-imaging," *Science (New York, N.Y.)*, vol. 318, p. 1750, Dec. 2007.

[60] J. Laverock, A. Preston, D. Newby, K. Smith, S. Sallis, L. Piper, S. Kittiwatanakul, J. Lu, S. Wolf, M. Leandersson, and T. Balasubramanian, "Photoemission evidence for crossover from Peierls-like to Mott-like transition in highly strained VO_2," *Physical Review B*, vol. 86, p. 195124, Nov. 2012.

[61] J. H. Park, J. M. Coy, T. S. Kasirga, C. Huang, Z. Fei, S. Hunter, and D. H. Cobden, "Measurement of a solid-state triple point at the metalinsulator transition in VO_2," *Nature*, vol. 500, pp. 431–434, Aug. 2013.

[62] S. Biermann, A. Poteryaev, A. Lichtenstein, and A. Georges, "Dynamical Singlets and Correlation-Assisted Peierls Transition in VO_2," *Physical Review Letters*, vol. 94, p. 026404, Jan. 2005.

[63] R. M. Wentzcovitch, W. W. Schulz, and P. B. Allen, "VO_2: Peierls or Mott-Hubbard? A View from Band Theory," *Physical Review Letters*, vol. 72, no. 21, pp. 3389–3392, 1994.

[64] Y.-G. Jeong, H. Bernien, J.-S. Kyoung, H.-R. Park, H.-S. Kim, J.-W. Choi, B.-J. Kim, H.-T. Kim, K. J. Ahn, and D.-S. Kim, "Electrical control of terahertz nano antennas on VO_2 thin film," *Optics Express*, vol. 19, no. 22, pp. 21211–21215, 2011.

[65] M. D. Goldflam, T. Driscoll, D. Barnas, O. Khatib, M. Royal, N. M. Jokerst, D. R. Smith, B.-J. Kim, G. Seo, H.-T. Kim, and D. N. Basov, "Two-dimensional reconfigurable gradient index memory metasurface," *Applied Physics Letters*, vol. 102, p. 224103, 2013.

[66] M. Nakano, K. Shibuya, D. Okuyama, T. Hatano, S. Ono, M. Kawasaki, Y. Iwasa, and Y. Tokura, "Collective bulk carrier delocalization driven by electrostatic surface charge accumulation," *Nature*, vol. 487, pp. 459–462, July 2012.

[67] M. Liu, H. Y. Hwang, H. Tao, A. C. Strikwerda, K. Fan, G. R. Keiser, A. J. Sternbach, K. G. West, S. Kittiwatanakul, J. Lu, S. A. Wolf, F. G. Omenetto, X. Zhang, K. A. Nelson, and R. D. Averitt, "Terahertz-field-induced insulator-to-metal transition in vanadium dioxide metamaterial.," *Nature*, vol. 487, pp. 345–8, July 2012.

[68] M. K. Liu, M. Wagner, E. Abreu, S. Kittiwatanakul, A. McLeod, Z. Fei, M. Goldflam, S. Dai, M. M. Fogler, J. Lu, S. A. Wolf, R. D. Averitt, and D. N. Basov, "Anisotropic Electronic State via Spontaneous Phase Separation in Strained Vanadium Dioxide Films," *Physical Review Letters*, vol. 111, p. 096602, Aug. 2013.

[69] E. Abreu, M. Liu, J. Lu, K. G. West, S. Kittiwatanakul, W. Yin, S. A. Wolf, and R. D. Averitt, "THz spectroscopy of VO_2 epitaxial films: controlling the anisotropic properties through strain engineering," *New Journal of Physics*, vol. 14, p. 083026, Aug. 2012.

[70] M. Wagner, Z. Fei, A. S. McLeod, A. S. Rodin, W. Bao, E. G. Iwinski, Z. Zhao, M. Goldflam, M. Liu, G. Dominguez, M. Thiemens, M. M. Fogler, A. H. Castro Neto, C. N. Lau, S. Amarie, F. Keilmann, and D. N. Basov, "Ultrafast and nanoscale plasmonic phenomena in exfoliated graphene revealed by infrared pump-probe nanoscopy.," *Nano letters*, vol. 14, pp. 894–900, Feb. 2014.

[71] Z. Q. Li, E. A. Henriksen, Z. Jiang, Z. Hao, M. C. Martin, P. Kim, H. L. Stormer, and D. N. Basov, "Dirac charge dynamics in graphene by infrared spectroscopy," *Nature Physics*, vol. 4, pp. 532–535, June 2008.

[72] A. J. Frenzel, C. H. Lui, W. Fang, N. L. Nair, P. K. Herring, P. Jarillo-Herrero, J. Kong, and N. Gedik, "Observation of suppressed terahertz absorption in photoexcited graphene," *Applied Physics Letters*, vol. 102, no. 11, p. 113111, 2013.

[73] A. N. Grigorenko, M. Polini, and K. S. Novoselov, "Graphene plasmonics," *Nature Photonics*, vol. 6, no. November, pp. 749–758, 2012.

[74] Z. Fei, A. S. Rodin, G. O. Andreev, W. Bao, A. S. McLeod, M. Wagner, L. M. Zhang, Z. Zhao, M. Thiemens, G. Dominguez, M. M. Fogler, A. H. Castro Neto, C. N. Lau, F. Keilmann, and D. N. Basov, "Gate-tuning of graphene plasmons revealed by infrared nano-imaging.," *Nature*, vol. 487, pp. 82–5, July 2012.

[75] A. K. Geim and K. S. Novoselov, "The rise of graphene.," *Nature materials*, vol. 6, pp. 183–91, Mar. 2007.

[76] J. Xue, J. Sanchez-Yamagishi, D. Bulmash, P. Jacquod, A. Deshpande, K. Watanabe, T. Taniguchi, P. Jarillo-Herrero, and B. J. LeRoy, "Scanning tunnelling microscopy and spectroscopy of ultra-flat graphene on hexagonal boron nitride.," *Nature materials*, vol. 10, pp. 282–5, Apr. 2011.

[77] G. Ahn, H. R. Kim, T. Y. Ko, K. Choi, K. Watanabe, T. Taniguchi, B. H. Hong, and S. Ryu, "Optical probing of the electronic interaction between graphene and hexagonal boron nitride.," *ACS nano*, vol. 7, pp. 1533–41, Feb. 2013.

[78] Y. Zheng, G.-X. Ni, C.-T. Toh, C.-Y. Tan, K. Yao, and B. Özyilmaz, "Graphene Field-Effect Transistors with Ferroelectric Gating," *Physical Review Letters*, vol. 105, p. 166602, Oct. 2010.

[79] Y. Zheng, G.-X. Ni, S. Bae, C.-X. Cong, O. Kahya, C.-T. Toh, H. R. Kim, D. Im, T. Yu, J. H. Ahn, B. H. Hong, and B. Özyilmaz, "Wafer-scale graphene/ferroelectric hybrid devices for low-voltage electronics," *EPL (Europhysics Letters)*, vol. 93, p. 17002, Jan. 2011.

[80] Y. Zheng, G.-X. Ni, C.-T. Toh, M.-G. Zeng, S.-T. Chen, K. Yao, and B. Ozyilmaz, "Gate-controlled nonvolatile graphene-ferroelectric memory," *Applied Physics Letters*, vol. 94, no. 16, p. 163505, 2009.

[81] X. Hong, A. Posadas, K. Zou, C. Ahn, and J. Zhu, "High-Mobility Few-Layer Graphene Field Effect Transistors Fabricated on Epitaxial Ferroelectric Gate Oxides," *Physical Review Letters*, vol. 102, pp. 2–5, Apr. 2009.

[82] S. Jandhyala, G. Mordi, D. Mao, M.-W. Ha, M. A. Quevedo-Lopez, B. E. Gnade, and J. Kim, "Graphene-ferroelectric hybrid devices for multi-valued memory system," *Applied Physics Letters*, vol. 103, no. 2, p. 022903, 2013.

[83] D. Jin, A. Kumar, K. Hung Fung, J. Xu, and N. X. Fang, "Terahertz plasmonics in ferroelectric-gated graphene," *Applied Physics Letters*, vol. 102, no. 20, p. 201118, 2013.

[84] A. Rajapitamahuni, J. Hoffman, C. Ahn, and X. Hong, "Examining Graphene Field Effect Sensors for Ferroelectric Thin Film Studies," *Nano letters*, vol. 13, pp. 4374–4379, 2013.

[85] M. H. Yusuf, B. Nielsen, M. Dawber, and X. Du, "Extrinsic and intrinsic charge trapping at the graphene/ferroelectric interface.," *Nano letters*, vol. 14, pp. 5437–44, Sept. 2014.

[86] C. Baeumer, S. Rogers, R. Xu, L. Martin, and M. Shim, "Tunable Carrier Type and Density in Graphene/$PbZr_{0.2}Ti_{0.8}O_3$ Hybrid Structures through Ferroelectric Switching," *Nano letters*, vol. 13, pp. 1693–1698, 2013.

[87] X. Hong, K. Zou, A. M. Dasilva, C. H. Ahn, and J. Zhu, "Integrating functional oxides with graphene," *Solid State Communications*, vol. 152, no. 15, pp. 1365–1374, 2012.

[88] M. Strikha, "Modulation of mid-IR radiation by a gated graphene on ferroelectric substrate," *Ukrainian Journal of Physical Optics*, vol. 12, no. 4, p. 161, 2011.

[89] F. Keilmann and R. Hillenbrand, "Near-field Microscopy by Elastic Light Scattering from a Tip," *Philosophical Transactions: Mathematical, Physical and Engineering Sciences*, pp. 787–805, 2004.

[90] M. Brehm, A. Schliesser, F. Cajko, I. Tsukerman, and F. Keilmann, "Antenna-mediated back-scattering efficiency in infrared near-field microscopy.," *Optics express*, vol. 16, pp. 11203–15, July 2008.

[91] D. A. Bonnell, D. N. Basov, M. Bode, U. Diebold, S. V. Kalinin, V. Madhavan, L. Novotny, M. Salmeron, U. D. Schwarz, and P. S. Weiss, "Imaging physical phenomena with local probes: From electrons to photons," *Reviews of Modern Physics*, vol. 84, pp. 1343–1381, Sept. 2012.

[92] Z. Fei, A. S. Rodin, G. Gannet, S. Dai, W. Regan, M. Wagner, M. K. Liu, A. S. McLeod, G. Dominguez, M. Thiemens, A. H. Castro-Neto, F. Keilmann, A. Zettl, R. Hillenbrand, M. M. Fogler, and D. N. Basov, "Electronic and plasmonic phenomena at graphene grain boundaries," *Nature nanotechnology*, vol. 8, no. November, pp. 821–825, 2013.

[93] N. Ocelic, A. Huber, and R. Hillenbrand, "Pseudoheterodyne detection for background-free near-field spectroscopy," *Applied Physics Letters*, vol. 89, no. 10, p. 101124, 2006.

[94] A. J. Huber, N. Ocelic, and R. Hillenbrand, "Local excitation and interference of surface phonon polaritons studied by near-field infrared microscopy.," *Journal of microscopy*, vol. 229, pp. 389–95, Mar. 2008.

[95] Z. Fei, G. O. Andreev, W. Bao, L. M. Zhang, A. S McLeod, C. Wang, M. K. Stewart, Z. Zhao, G. Dominguez, M. Thiemens, M. M. Fogler, M. J. Tauber, A. H. Castro-Neto, C. N. Lau, F. Keilmann, and D. N. Basov, "Infrared nanoscopy of dirac plasmons at the graphene-SiO_2 interface.," *Nano letters*, vol. 11, pp. 4701–5, Nov. 2011.

[96] J. Chen, M. Badioli, P. Alonso-González, S. Thongrattanasiri, F. Huth, J. Osmond, M. Spasenović, A. Centeno, A. Pesquera, P. Godignon, A. Z. Elorza, N. Camara, F. J. García de Abajo, R. Hillenbrand, and F. H. L. Koppens, "Optical nano-imaging of gate-tunable graphene plasmons.," *Nature*, vol. 487, pp. 77–81, July 2012.

[97] J. M. Caridad, F. Rossella, V. Bellani, M. Maicas, M. Patrini, and E. Diez, "Effects of particle contamination and substrate interaction on the Raman response of unintentionally doped graphene," *Journal of Applied Physics*, vol. 108, no. 8, p. 084321, 2010.

[98] C. Casiraghi, A. Hartschuh, H. Qian, S. Piscanec, C. Georgi, A. Fasoli, K. S. Novoselov, D. M. Basko, and A. C. Ferrari, "Raman spectroscopy of graphene edges.," *Nano letters*, vol. 9, pp. 1433–41, Apr. 2009.

[99] S. Dai, Z. Fei, Q. Ma, A. S. Rodin, M. Wagner, A. S. McLeod, M. K. Liu, W. Gannett, W. Regan, K. Watanabe, T. Taniguchi, M. Thiemens, G. Dominguez, A. H. Castro Neto, A. Zettl, F. Keilmann, P. Jarillo-Herrero, M. M. Fogler, and D. N. Basov, "Tunable phonon polaritons in atomically thin van der Waals crystals of boron nitride.," *Science (New York, N.Y.)*, vol. 343, pp. 1125–9, Mar. 2014.

[100] E. H. Hwang and S. Das Sarma, "Dielectric function, screening, and plasmons in two-dimensional graphene," *Physical Review B - Condensed Matter and Materials Physics*, vol. 75, no. 20, pp. 1–6, 2007.

[101] L. M. Zhang, G. O. Andreev, Z. Fei, A. S. McLeod, G. Dominguez, M. Thiemens, A. H. Castro-Neto, D. N. Basov, and M. M. Fogler, "Near-field spectroscopy of silicon dioxide thin films," *Physical Review B*, vol. 85, p. 075419, Feb. 2012.

[102] A. Woessner, M. B. Lundeberg, Y. Gao, A. Principi, P. Alonso-González, M. Carrega, K. Watanabe, T. Taniguchi, G. Vignale, M. Polini, J. Hone, R. Hillenbrand, and F. H. L. Koppens, "Highly confined low-loss plasmons in graphene-boron nitride heterostructures," *Nature Materials*, vol. 14, no. April, pp. 421–425, 2014.

[103] D. N. Basov, M. M. Fogler, A. Lanzara, F. Wang, and Y. Zhang, "Colloquium: Graphene spectroscopy," *Reviews of Modern Physics*, vol. 86, pp. 959–994, July 2014.

[104] I. Crassee, M. Orlita, M. Potemski, A. L. Walter, M. Ostler, T. Seyller, I. Gaponenko, J. Chen, and A. B. Kuzmenko, "Intrinsic terahertz plasmons and magnetoplasmons in large scale monolayer graphene.," *Nano letters*, vol. 12, pp. 2470–4, May 2012.

[105] R. Kimmel and A. Bruckstein, "Regularized Laplacian zero crossings as optimal edge integrators," *International Journal of Computer Vision*, vol. 53, no. 3, pp. 225–243, 2003.

[106] A. Frenzel, M. Qazilbash, M. Brehm, B.-G. Chae, B.-J. Kim, H.-T. Kim, A. Balatsky, F. Keilmann, and D. Basov, "Inhomogeneous electronic state near the insulator-to-metal transition in the correlated oxide VO_2," *Physical Review B*, vol. 80, pp. 1–7, Sept. 2009.

[107] R. Carminati and J.-J. Greffet, "Influence of dielectric contrast and topography on the near field scattered by an inhomogeneous surface," *Journal of the Optical Society of America A*, vol. 12, p. 2716, Dec. 1995.

[108] X. Hong, J. Hoffman, A. Posadas, K. Zou, C. H. Ahn, and J. Zhu, "Unusual resistance hysteresis in n-layer graphene field effect transistors fabricated on ferroelectric $Pb(Zr_{0.2}Ti_{0.8})O_3$," *Applied Physics Letters*, vol. 97, no. 3, p. 033114, 2010.

[109] G. Ni, Y. Zheng, S. Bae, C. Tan, O. Kahya, J. Wu, B. Hong, K. Yao, and B. Özyilmaz, "Graphene-ferroelectric hybrid structure for flexible transparent electrodes.," *ACS Nano*, vol. 6, no. 5, pp. 3935–3942, 2012.

[110] A. Gruverman, O. Auciello, and H. Tokumoto, "Scanning force microscopy for the study of domain structure in ferroelectric thin films," *Journal of Vacuum Science & Technology B*, vol. 14, no. 2, pp. 602–605, 1996.

[111] P. Paruch, T. Tybell, and J.-M. Triscone, "Nanoscale control of ferroelectric polarization and domain size in epitaxial $Pb(Zr_{0.2}Ti_{0.8})O_3$ thin films," *Applied Physics Letters*, vol. 79, no. 4, p. 530, 2001.

[112] T. Tybell, C. H. Ahn, and J.-M. Triscone, "Control and imaging of ferroelectric domains over large areas with nanometer resolution in atomically smooth epitaxial $Pb(Zr_{0.2}Ti_{0.8})O_3$ thin films," *Applied Physics Letters*, vol. 72, no. 12, p. 1454, 1998.

[113] C. Ahn, T. Tybell, L. Antognazza, K. Char, R. Hammond, M. Beasley, O. Fischer, and J.-M. Triscone, "Local, nonvolatile electronic writing of

epitaxial $Pb(Zr_{0.52}Ti_{0.48})O_3/SrRuO_3$ heterostructures," *Science*, vol. 276, pp. 1100–1103, May 1997.

[114] Y. Wang, C. Ganpule, B. T. Liu, H. Li, K. Mori, B. Hill, M. Wuttig, R. Ramesh, J. Finder, Z. Yu, R. Droopad, and K. Eisenbeiser, "Epitaxial ferroelectric $Pb(Zr,Ti)O_3$ thin films on Si using $SrTiO_3$ template layers," *Applied Physics Letters*, vol. 80, no. 1, p. 97, 2002.